Geochemistry, Geophysics, Geosystems®

AGU ADVANCING EARTH AND SPACE SCIENCE

RESEARCH ARTICLE
10.1029/2022GC010389

Changes in Plate Motions Caused by Increases in Gravitational Potential Energy of Mountain Belts

Philip England[1] **and Peter Molnar**[2†]

[1]Department of Earth Sciences, University of Oxford, Oxford, UK, [2]CIRES and Department of Geological Sciences, University of Colorado Boulder, Boulder, CO, USA

Abstract Reconstructions of motions of the Nazca, South American, and Indian plates record short-duration (≲10 Myr) variations in angular velocity, which enable a vector-based test of the hypothesis that mountain uplift can cause changes in plate motion. Reductions in velocity of Nazca and South America between ∼12 and 6 Ma coincide with a phase of rapid surface uplift in the Central Andes. Decrease in the rate of India's convergence with Eurasia between ∼20 and 10 Ma corresponds to an increase in gravitational potential energy per unit area (GPE) within Tibet, marked by a transition from crustal thickening to thinning. The vectorial test shows that, in each case, the only change in driving force capable of balancing the change in basal drag is an increased resistance along the convergent boundary to the plate. Changes in GPE associated with mountain uplift provide a calibration for basal drags on plates. Basal tractions of ∼0.1–1 MPa provide resisting forces comparable in magnitude to driving forces from GPE variation in ocean lithosphere. The rapid change in motion of the Indian plate between about 48 and 41 Ma is explained by the juxtaposition of the Indian continent against the Andean-type margin of the Transhimalaya and reduction in driving force due to loss of the slab. The net slab driving force lost was ∼2–4 TN m^{-1}, in agreement with previous studies suggesting that forces resisting slabs' penetration into the mantle largely offset their negative buoyancy.

1. Introduction

The goal of this study is to test the hypothesis that changes in gravitational potential energy per unit area (GPE) associated with the uplift of mountain belts influence the motions of plates. We focus on three episodes of rapid reduction in the convergence of plates that bound mountain ranges: a decrease of ∼40 mm/yr in Nazca-South America convergence between ∼12 and 6 Ma, and reductions in India-Eurasia convergence by about 20 mm/yr between ∼20 and 10 Ma, and by about 100 mm/yr between ∼48 and 41 Ma. The first two of these events have been attributed to rapid increases in GPE of, respectively, the Andes and Tibet (e. g. Garzione et al., 2006; Heidbach et al., 2008; Iaffaldano et al., 2006; Molnar & Stock, 2009; Norabuena et al., 1999). The reduction of rate of convergence between India and Asia in Eocene time has been attributed to changes in plate driving forces (e. g., Molnar & Tapponnier, 1975; Patriat & Achache, 1984) and to change in GPE associated with thickening of the crust of Tibet (Copley et al., 2010).

Previous investigations of the relation between plate motions and changes in the GPE of mountains have taken one of two forms. Some authors have relied upon the temporal coincidence of a change in angular velocity of a plate and geological evidence consistent with increase in GPE of a mountain belt at the edge of the plate (e. g. Garzione et al., 2006; Molnar & Stock, 2009; Norabuena et al., 1999); this approach does not directly address the dynamics. Others employ numerical modeling of several interacting processes (e.g. Austermann et al., 2011; Forte et al., 2009; Heidbach et al., 2008; Iaffaldano et al., 2006) the drawback of that approach is that the calculations have many adjustable parameters, and it is difficult to ascertain the uniqueness of preferred solutions. We use recent high-resolution reconstructions of plate motion (DeMets & Merkouriev, 2019, 2021) to calculate changes in torque due to changes in basal drag on the relevant plates. The assumption that those changes were balanced by changes in boundary tractions allows us to carry out a simple vectorial test of the hypothesis, and to place bounds on the basal drag on the plates, and on the difference between negative buoyancy of the slabs and the frictional or viscous resistance to their motions.

†Deceased.

Key Points:

- Calculation of forces required to cause rapid changes in plate motion test the hypothesis that some stem from increase in gravitational potential energy (GPE) of mountains
- Rapid decreases in velocity of Nazca, South American, and Indian plates require increases in resistance at their convergent boundaries
- Geological evidence shows that the Miocene decreases in velocity were contemporaneous with increases in GPE of the Andes and Tibet

Correspondence to:
P. England,
philip.england@earth.ox.ac.uk

Citation:
England, P., & Molnar, P. (2022). Changes in plate motions caused by increases in gravitational potential energy of mountain belts. *Geochemistry, Geophysics, Geosystems*, *23*, e2022GC010389. https://doi.org/10.1029/2022GC010389

Received 15 FEB 2022
Accepted 23 AUG 2022

Author Contributions:
Conceptualization: Philip England, Peter Molnar
Methodology: Philip England, Peter Molnar
Writing – original draft: Philip England
Writing – review & editing: Peter Molnar

2. Method

2.1. Rapid Changes in Forces on Plates

We analyze the differences between forces acting on plates at two times, separated by 10 million years or less, over which interval their angular velocities changed significantly. We now discuss which of the principal types of force acting on the plates are capable of effecting a change in plate motion on such time scales.

A force arises from the diminution of the GPE of the oceanic lithosphere as it ages, and acts in the direction of increasing age. Although this force is often referred to as "ridge push," and is commonly shown schematically as acting at the ridges, it is determined by the density structure of all the oceanic portions of a plate and is better thought of as a force distributed across the whole plate (e.g., Lister, 1975). Because this density structure is set up over the lifetime of the plate, it is incapable of generating a rapid change in plate motion, even were the location of a spreading ridge to change rapidly.

Richards and Lithgow-Bertelloni (1996) suggested that rapid change in plate motion could reflect the creation or destruction of major transform faults, but no such change affected the plates we consider at the times of interest.

The net force at convergent margins is the sum of the force due to the negative buoyancy of the subducting plate, usually referred to as "slab pull," and the resistance to convergence by tractions on the plate boundary and by viscous forces due to the relative motions of slab and its surrounding upper mantle. This balance may change on the time scale of a few million years if part of the slab detaches (Isacks et al., 1968), or if the age of ocean floor entering the trench changes rapidly.

Changes in force balance at convergent margins also arise from increases in the GPE of the overriding plate during mountain building; although some of the change in GPE will be supported by changes in deviatoric stress within the mountain belt we should, in general, expect an increase in the compressional force per unit length on the surroundings to the mountain belt (e.g., Molnar & Lyon-Caen, 1988). When such increases are proximal to convergent boundaries, they are presumably balanced by increased traction on, and/or increased down-dip extent of, the plate boundary and so act to increase resistance to convergence. Changes in crustal thickness by horizontal shortening and vertical thickening of the lithosphere occur over timescales of tens of millions of years, and have been invoked to explain changes in plate motion on such time scales (e.g., Copley et al., 2010).

Increases in GPE of mountain belts can also occur via the replacement of cool mantle lithosphere, and/or eclogitic lower crust, by asthenosphere (e.g., Bird, 1979; England & Houseman, 1989; Jull & Kelemen, 2001; Kay & Mahlburg Kay, 1991; Molnar et al., 1993; Nelson, 1992). The resultant increase in GPE of the lithosphere may be as great as ~4–8 TN m^{-1}—larger than the ridge push (see England and Houseman (1989), Garzione et al. (2006), Molnar et al. (1993), Molnar and Stock (2009) and Appendix B for discussion). Furthermore, these changes are likely to take place on the time scale of one to a few million years (e.g., Conrad & Molnar, 1997, 1999; Houseman & Molnar, 1997; Houseman et al., 1981; Jull & Kelemen, 2001; Molnar et al., 1998).

Both kinematic calculations (e.g., Chapple & Tullis, 1977; Forsyth & Uyeda, 1975) and global dynamical models (e.g., Hager & O'Connell, 1981; Lithgow-Bertelloni & Richards, 1995, 1998), show the dominant driving forces for plate motion to be those associated with density variations in oceanic lithosphere and with the slabs. However, variations in GPE per unit area due to mantle convection may locally affect force balances (e.g., Lithgow-Bertelloni & Silver, 1998), and such changes may occur within a few million years during the impingement of a plume head on the base of the lithosphere (e.g., Cande & Stegman, 2011; van Hinsbergen et al., 2011). The basal tractions and increased GPE associated with plumes are likely to vary radially from the center of the plume; in consequence, we should not expect a plume to influence motions appreciably unless it is close to the edge of a plate.

2.2. Changes in Basal Drag

Our calculations address changes in angular velocities of the plates over a few million years, and we make the assumption that the distribution of velocities in the mantle below the asthenosphere does not change appreciably on that time scale, so that the associated changes in basal drag are antiparallel to the change in velocity, regardless of the orientation of the total drag. We are impelled to this assumption because, although a change in motion of one plate must involve changes in the motion within the whole mantle, the myriad uncertainties in the structures of density and viscosity within the mantle ensure that departures from the assumption cannot be calculated with any precision, or accuracy.

We assume a constitutive relationship for the mantle below the plate of the form

$$\tau_{ij} = B\dot{E}^{\left(\frac{1}{n}-1\right)}\dot{\varepsilon}_{ij} \tag{1}$$

where $\dot{\varepsilon}_{ij}$ is the ij th component of the strain-rate tensor, τ_{ij} is the ij th component of the deviatoric stress, and

$$\dot{E} = \frac{1}{\sqrt{2}}(\dot{\varepsilon}_{kl}\dot{\varepsilon}_{kl})^{\frac{1}{2}} \tag{2}$$

is the second invariant of the strain-rate tensor of the fluid, assumed incompressible, and the convention of summation over repeated indices applies. This relation allows either for a power-law dependence of strain rate on stress, as would be the case if deformation in the asthenosphere were dominated by dislocation creep, or for Newtonian viscosity ($n = 1$), as would be the case for diffusion creep. For calculations with non-Newtonian viscosity we use $n = 3.5$, which is appropriate for the dislocation creep of olivine (e.g. Hirth & Kohlstedt, 2003).

We treat velocities beneath each plate as having a single component, v_x, in the local direction of motion of the plate with respect to the reference frame. Equations 1 and 2 reduce to

$$\dot{E} = \dot{\varepsilon}_{xz} = \frac{1}{2}\frac{\partial v_x}{\partial z} \tag{3}$$

$$\tau = \tau_{xz} = B\dot{\varepsilon}_{xz}^{\frac{1}{n}} = \frac{B}{2^{1/n}}\left(\frac{\partial v_x}{\partial z}\right)^{\frac{1}{n}}, \tag{4}$$

where z is upward, and we take the base of the plate to be at $z = 0$. With this configuration of flow, τ is independent of depth, and both τ and $\partial v_x/\partial z$ are positive throughout $0 > z > -\infty$.

Laboratory determinations of rheological parameters of minerals are often expressed as

$$\dot{\varepsilon} \propto \tau^n \exp\left(-\frac{Q + pV^*}{RT}\right), \tag{5}$$

where T is absolute temperature, R is the gas constant Q is an activation energy for the deformation mechanism, and V^* expresses the influence of pressure, p. We make the approximation that temperature in the asthenosphere has a constant value, T_a, which gives

$$\frac{\partial v_x}{\partial z} \propto \tau^n \exp\left(\frac{-Q}{RT_a}\right)\exp\left(\frac{\rho g z V^*}{RT_a}\right) = \left(\frac{\tau}{B_0}\right)^n \exp\left(\frac{z}{D}\right), \tag{6}$$

where

$$D = \frac{RT_a}{g\rho V^*}, \tag{7}$$

and B_0 expresses the dependence of effective viscosity at the base of the plate on activation energy and temperature.

The conditions $v(z = 0) = v_0$; $v \to 0$ as $z \to -\infty$ give

$$v_x = v_0 \exp\left(\frac{z}{D}\right), \tag{8}$$

$$v_0 = D\left(\frac{\tau}{B_0}\right)^n, \tag{9}$$

where v_0 is the local speed of the plate relative to the deep mantle.

The shear stress at the base of the plate is

$$\tau_0 = B_0\left(\frac{\partial v_x}{\partial z}\right)_{z=0}^{1/n} = B_0\left(\frac{v_0}{D}\right)^{1/n}, \tag{10}$$

from which we see that, for a Newtonian asthenosphere, B_0 is the viscosity at its top. We estimate D, in the Newtonian case, by assuming $V^* \sim 10^{-5}$ m^3/mol, (the middle of the range for diffusion creep given by Hirth & Kohlstedt, 2003) and $T \sim 1600$ K; then $D \sim 40$ km. For non-Newtonian asthenosphere, the material property constrained by our analysis is $B_0/D^{1/n}$, which is independent of v_0. The activation volume for dislocation creep measured by Dixon and Durham (2018) is $V^* = 15 \pm 5 \times 10^{-6}$ m^3/mol.

The change in traction on the base of the plate, $\mathbf{\Delta\sigma}$, as a result of change in velocity, $\mathbf{\Delta v}$, depends upon the rheological parameters of the substrate. For Newtonian asthenosphere

$$\mathbf{\Delta\sigma} \approx -\frac{B_0}{D}\mathbf{\Delta v}. \tag{11}$$

For a power-law asthenosphere

$$\mathbf{\Delta\sigma} \approx -\frac{B_0}{D^{1/n}}\left(|\boldsymbol{v}_2|^{1/n}\,\hat{\boldsymbol{v}}_2 - |\boldsymbol{v}_1|^{1/n}\,\hat{\boldsymbol{v}}_1\right), \tag{12}$$

where the hats denote unit velocities, and subscripts 1 and 2 denote the beginning and end of the time interval over which the velocity changed. In writing Equations 11 and 12, we have assumed that the viscosity is horizontally isotropic. The approximation symbols denote that we have neglected changes in motion of the deep mantle over short time intervals. In what follows we treat Equations 11 and 12 as equalities.

The change in torque on the plate due to the change in its angular velocity is

$$\mathbf{\Delta T}_p = \int_A \boldsymbol{r} \times \mathbf{\Delta\sigma}\,\mathrm{d}A. \tag{13}$$

Torques are calculated with the plates in their positions at each time of interest; therefore the contribution of each element, dA, to the total torque depends on the reference frame in which the velocity difference is calculated. Furthermore, for a non-Newtonian substrate, the choice of reference frame influences the calculation of $\mathbf{\Delta\sigma}$ in Equation 12.

Because of the uncertainties in the viscosity structure of the upper mantle, none of B_0, D, and n can be specified a priori. So, it is appropriate to consider dimensionless quantities:

$$\begin{aligned}
\boldsymbol{v}' &= \frac{t_0\,\boldsymbol{v}}{R} = \frac{t_0|\boldsymbol{v}|\,\hat{\boldsymbol{v}}}{R} \\
\hat{\boldsymbol{r}} &= \frac{\boldsymbol{r}}{R}; \quad A' = \frac{A}{R^2} \\
\boldsymbol{T}'_p &= \boldsymbol{T}_p \frac{1}{B_0 R^3}\left(\frac{t_0 D}{R}\right)^{1/n} \\
\boldsymbol{F}'_b &= \boldsymbol{F}_b \frac{1}{B_0 R^2}\left(\frac{t_0 D}{R}\right)^{1/n}
\end{aligned} \tag{14}$$

where the hats denote unit vectors, $\boldsymbol{F}_b$ is a force per unit length acting on a plate boundary, and R is the radius of the Earth. We choose the time scale t_0 to be 1 Myr: the changes in plate speed, $\mathbf{\Delta}|\boldsymbol{v}|$, we consider are of order 10 s of mm/yr and, as discussed above, D is of order tens of kilometers. So characteristic strain rates are of order Myr^{-1}.

Equation 13 becomes

$$\mathbf{\Delta T}'_p = \int_{A'} \hat{\boldsymbol{r}} \times \left(|\boldsymbol{v}'_1|^{1/n}\,\hat{\boldsymbol{v}}_1 - |\boldsymbol{v}'_2|^{1/n}\,\hat{\boldsymbol{v}}_2\right)\mathrm{d}A'. \tag{15}$$

Consider a segment of the boundary to the plate, at position $\hat{\boldsymbol{r}}_b$, and suppose that a change in dimensionless force, $\mathbf{\Delta F}'_b$, on this segment balances the change in dimensionless torque due to change in basal drag, $\mathbf{\Delta T}'_p$. Then

$$\mathbf{\Delta T}'_p = -\hat{\boldsymbol{r}}_b \times \mathbf{\Delta F}'_b. \tag{16}$$

$\mathbf{\Delta F}'_b$ acts horizontally, so $\mathbf{\Delta F}'_b \cdot \hat{\boldsymbol{r}}_b = 0$. The cross product of Equation 16 with $\hat{\boldsymbol{r}}_b$ gives

$$-\Delta \boldsymbol{T}'_p \times \hat{\boldsymbol{r}}_b = \hat{\boldsymbol{r}}_b \times \Delta \boldsymbol{F}'_b \times \hat{\boldsymbol{r}}_b \tag{17}$$

$$= \Delta \boldsymbol{F}'_b (\hat{\boldsymbol{r}}_b \cdot \hat{\boldsymbol{r}}_b) - \hat{\boldsymbol{r}}_b \left(\Delta \boldsymbol{F}'_b \cdot \hat{\boldsymbol{r}}_b\right) \tag{18}$$

$$\Delta \boldsymbol{F}'_b = \Delta \boldsymbol{T}'_p \times \hat{\boldsymbol{r}}_b. \tag{19}$$

Equations 14 and 19 show how the unknown quantities, B_0, D, and n, are related to the dimensionless torque, and to changes in boundary forces:

$$R\Delta F_b = \Delta T_p \sin\phi = B_0 R^3 \left(\frac{R}{t_0 D}\right)^{1/n} \Delta T'_p \sin\phi \tag{20}$$

$$\frac{B_0}{D^{1/n}} = \frac{\Delta F_b}{\Delta T'_p \sin\phi R^2} \left(\frac{t_0}{R}\right)^{1/n}, \tag{21}$$

$$\overline{\Delta\sigma} = \frac{\Delta F_b}{A}. \tag{22}$$

where $\Delta F_b = |\Delta \boldsymbol{F}_b|$, $\Delta T_p = |\Delta \boldsymbol{T}_p|$, and $\overline{\Delta\sigma}$ is the average change in basal traction on the plate, of area A, and ϕ is the angle between the torque and radius vectors. In practice, $\sin\phi \approx 1$ for all the cases we consider, and is not mentioned again.

3. Late-Cenozoic Changes in Plate Motion

We use the framework established above to analyze the changes in angular velocity listed in Table 1. We choose the Nubian plate as the reference frame for changes in the motions of the South American and Nazca pates, and Eurasia for changes in motion of the Indian plate. To illustrate the influence of choice of reference frame, we also calculate changes in torque for the Nazca and South American plates in the present-day no-net-rotation frame of NNR-MORVEL56 (Argus et al., 2011). We defer discussion of the uncertainties in our calculations to Section 5 because the relations between epistemic and aleatoric uncertainties are more clearly seen after the calculations have been presented.

For each time interval of interest we calculate the change in dimensionless torque on the plate associated with the change in its angular velocity (Equation 15). We then determine, for each segment of the boundary to the plate, the change in dimensionless force that would be required to balance the change in dimensionless torque (Equation 19). Some combinations of change in force and orientation of boundary are implausible, from the arguments of Section 2.1 (e.g., shear forces parallel to ridges, or reductions in ridge push), but forces acting approximately normal to a divergent or convergent boundary would be plausible. We also evaluate the possible role of tractions associated with hotspots.

3.1. Post-12 Ma Changes in Nazca-Nubia and South America-Nubia Relative Motions

Several studies have reported a slowing of Nazca-South America convergence over the past ~10 Ma (e.g. Garzione et al., 2006; Heidbach et al., 2008; Iaffaldano & Bunge, 2009; Iaffaldano et al., 2006; Norabuena et al., 1999), when several lines of evidence, reviewed Section 3.2, suggest that surface elevations in at least parts of the Central Andes increased. In particular, Garzione et al. (2006) suggested that an abrupt slowing of the rate of convergence between the Nazca and South American plates between 9 and 6 Ma was caused by uplift of the Bolivian Altiplano by 2,000–3,000 m. We test this suggestion by identifying the forces that can plausibly explain the changes in angular velocity of the South American and Nazca plates around this time.

The rate of motion of Nazca with respect to Nubia dropped from 110 to 40 mm/yr after ~12 and before 6 Ma (Garzione et al., 2006; Appendix A1, and Figure 1a), and the rate of motion of South America dropped from 49 to 33 mm/yr (DeMets & Merkouriev, 2019, and Figure 1c). In order to compare changes in torques on the plates we need to choose stage angular velocities that both are representative of the time intervals bracketing the change and, insofar as is possible, are synchronous between plates. From the data available to us at present we represent

Table 1
Changes in Angular Velocity, $\boldsymbol{\Delta\omega}$, of the Nazca, South American, Indian and Nubian Plates, and Resulting Changes in Dimensionless Torques Due To Basal Drag, $\boldsymbol{\Delta T'_p}$

	Longitude °E	Latitude °N	Magnitude	$\overline{\Delta\lvert v\rvert^{1/n}}$ $\left(\text{mm yr}^{-1}\right)^{1/n}$	ΔF_b N	$B_0/D^{1/n}$ Pa $(\text{s/m})^{1/n}$
	Nazca-Nubia post-12 Ma[a]			$A = 16 \times 10^6$ km^2	$\underline{6 \times 10^{18}}$[b]	
$\boldsymbol{\Delta\omega}$	52.5	−75.8	0.56[c]			
$\boldsymbol{\Delta T'_p}, n = 1$, NU	64.1	−70.7	3.7×10^{-3}	59		2.0×10^{14}[d]
$\boldsymbol{\Delta T'_p}, n = 3.5$, NU	139.9	−65.8	3.8×10^{-2}	1.3		3.2×10^{8}[d]
$\boldsymbol{\Delta T'_p}, n = 3.5$, NNR	136.6	−65.9	9.4×10^{-2}	1.0		1.3×10^{8}[d]
	South America-Nubia post-12 Ma[e]			$A = 44 \times 10^6$ km^2	$\underline{6 \times 10^{18}}$[b]	
$\boldsymbol{\Delta\omega}$	−31.2	54.6	0.15[c]			
$\boldsymbol{\Delta T'_p}, n = 1$, NU	−26.1	65.8	2.5×10^{-3}	15		2.9×10^{14}[d]
$\boldsymbol{\Delta T'_p}, n = 3.5$, NU	−11.4	63.4	2.8×10^{-2}	0.5		4.3×10^{8}[d]
$\boldsymbol{\Delta T'_p}, n = 3.5$, NNR	−2.2	52.2	2.1×10^{-2}	0.6		5.7×10^{8}[d]
	India-Eurasia between 20 and 10 Ma[f]			$A = 21 \times 10^6$ km^2	$\underline{4 \times 10^{18}}$[b]	
$\boldsymbol{\Delta\omega}$	−157.5	−11.7	0.27[c]			
$\boldsymbol{\Delta T'_p}, n = 1$, EU	171.2	−20.6	1.9×10^{-3}	24		2.5×10^{14}[d]
$\boldsymbol{\Delta T'_p}, n = 3.5$, EU	175.7	12.3	2.2×10^{-2}	0.6		3.6×10^{8}[d]
	India-Eurasia between 48 and 41 Ma[f]			$A = 22 \times 10^6$ km^2		
$\boldsymbol{\Delta\omega}$	−154.6	0.8	1.3[c]			
$\boldsymbol{\Delta T'_p}, n = 1$, EU	172.1	−11.9	8.6×10^{-3}	101	10^{19}[g]	$\underline{2 \times 10^{14}}$[h]
$\boldsymbol{\Delta T'_p}, n = 3.5$, EU	178.3	20.0	7.3×10^{-2}	1.8	10^{19}[g]	$\underline{4 \times 10^{8}}$[h]

Note. The value of n (Equation 1) and the frame of reference are given by each torque. $B_0/D^{1/n}$ is calculated from the magnitude of the change in boundary force, ΔF_b, or vice versa. In each case, the assumed value is underlined, and reasons for the assumption are given in the relevant section of the text; in some cases the calculated value differs from that obtained from the relevant tabulated quantities because of rounding.

[a]Garzione et al. (2006), NZ-SA, minus DeMets and Merkouriev (2019) NU–SA; Section 3.1, Figures 1 and 2. [b]Value assumed as discussed in relevant section of text. [c]Pole and magnitude of $\boldsymbol{\Delta\omega}$; rate in °/Myr, positive counter-clockwise. [d]Calculated from ΔF_b (Equation 21). [e]DeMets and Merkouriev (2019), Section 3.1, Figures 1 and 2. [f]DeMets and Merkouriev (2019), Section 4, Figures 4 and 5. [g]Calculated from estimated $B_0/D^{1/n}$ (Equation 21), and given to 1 significant figure. [h]As for 20–10 Ma, to one significant figure.

the change in motion of the South American plate by forming weighted averages of the stage angular velocities derived from the finite rotations of anomalies 5Ey–5An.2 and those from anomalies 3An.1–1n (Figure 1d); the weight for each angular velocity is the standard deviation of its magnitude (DeMets & Merkouriev, 2019, Table 2). For the Nazca plate, we average angular velocities derived from anomalies 5E–4A and from 2A to the present (Figure 1b) (Garzione et al., 2006, and Appendix A1, here). The angular velocities are derived by centered differencing: the finite rotation between Anomaly $n - 1$ and Anomaly $n + 1$ is divided by the time interval between them, and plotted at the middle of that interval. Those averages are unweighted because Garzione et al. (2006) did not report uncertainties in their reconstructions.

The changes in velocity of the plates relative to Nubia, over these time intervals, are shown in Figure 2. The blue arrows show the orientations of dimensionless forces, $\boldsymbol{\Delta F'_b}$, required to balance the changes in dimensionless torque on the plates, $\boldsymbol{\Delta T'_p}$ (Equation 19). Each arrow shows the orientation of the force required if that segment alone were to balance the change in dimensionless torque due to the change in basal drag on the plate. For example, if the change in basal drag on the South American plate is to be explained by a force acting in the neighborhood of point 10, that force is required to act in a southeasterly direction; if the force is to be in the region of point 8 then it must act eastward, and so on.

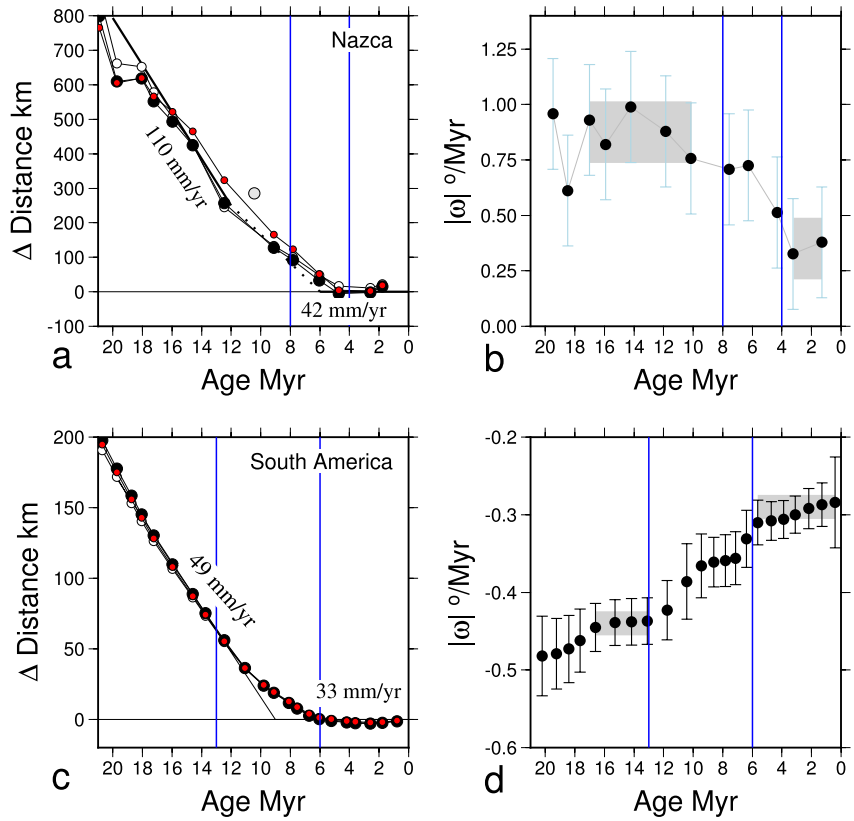

Figure 1. Variations with time of position and angular velocities of the Nazca and South American plates with respect to the Nubian plate. (a) Distances from their current positions of three points (points 4, 5, and 6 in Figure 2) on the Nazca side of the NZ–SA plate boundary; the distances are reduced by 32, 42, and 41 mm/yr for respectively, the open (Point 4), black (Point 5), and red (Point 6) circles. Finite rotations are from Garzione et al. (2006, and Appendix A1, here) and DeMets and Merkouriev (2019). The gray circle indicates displacement at anomaly-5 time, which we exclude, as discussed in Appendix A1. (b) Variations in magnitude of stage angular velocities; error bars show a nominal 0.25°/Myr uncertainty. Gray bands show the time intervals over which angular velocities are averaged to calculate the difference in torques across the time interval between the blue vertical lines. The distance plot in (c) is for the same three points as in (a), but on the South American side of the boundary. Distances are reduced by 31.5, 33, and 31 mm/yr for respectively, the open (Point 4), black (Point 5), and red (Point 6) circles. Finite rotations are from DeMets and Merkouriev (2019). (d) As for (b), for variations in magnitude of noise-reduced stage angular velocities of the South American plate (DeMets & Merkouriev, 2019); uncertainties are calculated from the covariance matrices of DeMets and Merkouriev (2019).

It is unlikely that the requisite forces could have arisen from the hotspots of the region. Figure 2 shows four hotspots beneath the Nazca plate, two on the South American plate, and one close to the South Atlantic ridge, from the compilation of Steinberger (2000). Because of their intraplate locations, tractions acting radially outwards from the Juan Fernandez, San Felix, Fernando, and Trindade hotspots are unlikely to produce net forces on the respective plates. In contrast, the Easter Island, Galapagos, and St Helena hotspots lie close to plate edges, and one can envisage net forces that arise from resolving approximately half of the radially-directed forces in the direction perpendicular to the relevant plate boundaries. The net force on the Nazca plate from the Galapagos hotspot would then act southward, and that from Easter Island would act eastward. By the same argument, the net force on the South American plate from the St Helena hotspot would act westward. None of those forces is a plausible cause of the change in plate motion, being perpendicular to the required force in the case of the Galapagos, and being antiparallel in the other two cases (Figure 2).

For most of the boundary segments, the required orientations of the forces are implausible, given the nature of the boundary. The required forces on the western edge of the Nazca plate (segment 1 to 3) and on the eastern edge of the South American plate (segment 8 to 9) correspond to reductions in ridge push. As discussed in Section 2.1, that would require changes in the thermal structure of the entire plate, which could not occur within a few million years. The relative motion along the transform-dominated Nazca-Antarctic boundary (segment 6 to 1) is predom-

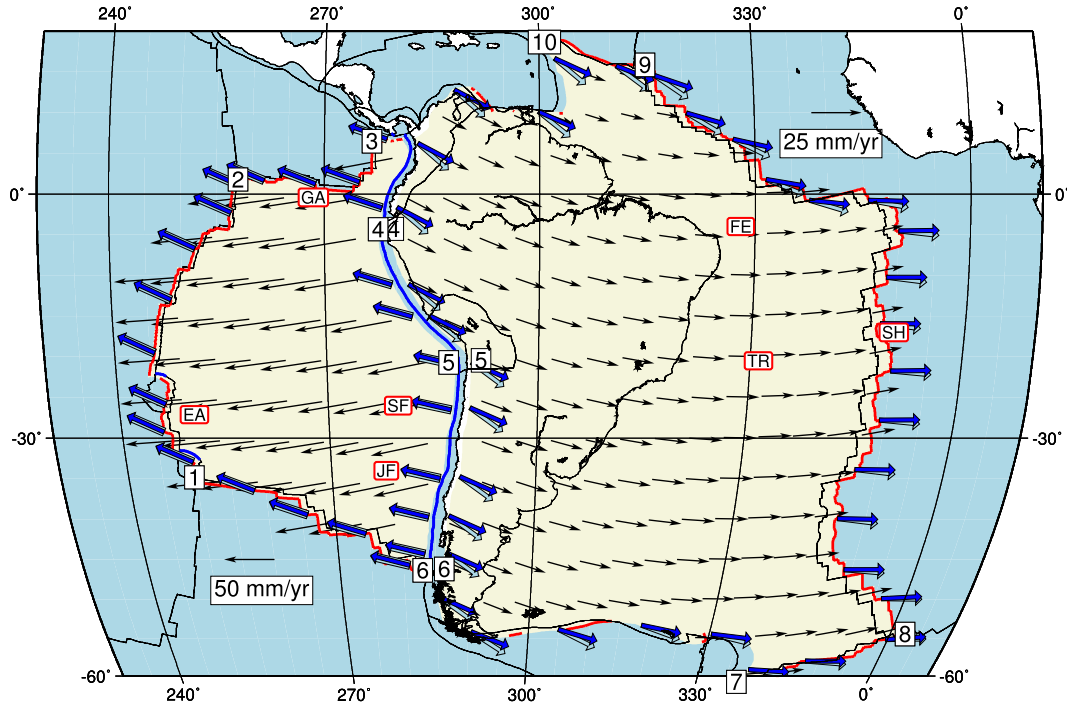

Figure 2. Changes in velocities of the Nazca and South American plates with respect to the Nubian plate, from the angular velocity differences given in Table 1. Oceanic ridges are shown in red; the location of the present Nazca-South America trench is shown in blue. Plates, and the vectors, are displayed in their positions at the ends of the intervals over which velocity changes are calculated. Dark blue arrows show orientations of changes in boundary forces that are capable of causing the changes in torques calculated from the angular velocity differences for a non-Newtonian asthenosphere, with motions relative to Nubia (rows labeled $n = 3.5$, NU in Table 1). Light blue arrows show force directions calculated with motions in the no-net-rotation frame (rows labeled $n = 3.5$, NNR in Table 1) in many places, these are very similar to the dark blue arrows, and have been shifted slightly to make them visible. Numbered points at locations on the present-day plate boundaries are used in the discussion of dimensionless forces acting along boundary segments (see text). Two-letter abbreviations show the locations of hotspots from the catalog of Steinberger (2000). From west to east, these are **EA**ster Island, **GA**lapagos, **J**uan **F**ernandez, **S**an **F**elix, **FE**rnando, **TR**indade, and **S**t **H**elena.

inantly right-lateral; the forces resisting that motion act approximately westward on the Nazca plate. If changes in force along this boundary are to generate the change in torque on the Nazca plate, they must represent an increase in the westward forces (blue arrows in Figure 2). No explanation for such a change suggests itself in the context of slowing right-lateral Nazca-Antarctica motion along that boundary. It is also hard to see how such a change could arise spontaneously. The same argument applies to the required increase in westward forces on the Nazca-Cocos boundary (Sections 2–3) and in eastward forces on South America at its southern boundary (Sections 6–8).

In contrast, the required changes in force along the Nazca-South America plate boundary are approximately perpendicular to that boundary for each plate. Furthermore, the calculated boundary forces are almost anti-parallel (Figure 3) and similar in magnitude (Table 1). These circumstances do not change if a different frame of reference is chosen, nor do they depend strongly on the choice of n (Figure 3). The difference in orientation of boundary force between calculations with $n = 3.5$ and those with $n = 1$ arises from the dependence of change in basal drag upon the $1/n$th power of the change in velocity, so the relative influences of different parts of the plate on the torque change as n changes. Taken together, these arguments strongly suggest that the changes in angular velocity of the Nazca and South American plates were caused by an increase in resisting force per unit length acting on each plate at the Nazca-South America plate boundary. We discuss the mechanisms that might have caused this increase in Section 3.3.

3.2. Changes in Elevation of the Andes

Evidence of rapid elevation changes in the Andes during the past 15 Ma derive from: (a) measurements of proxies that depend on elevation, such as $\delta^{18}O$ values in carbonate sediment or past surface temperatures from the

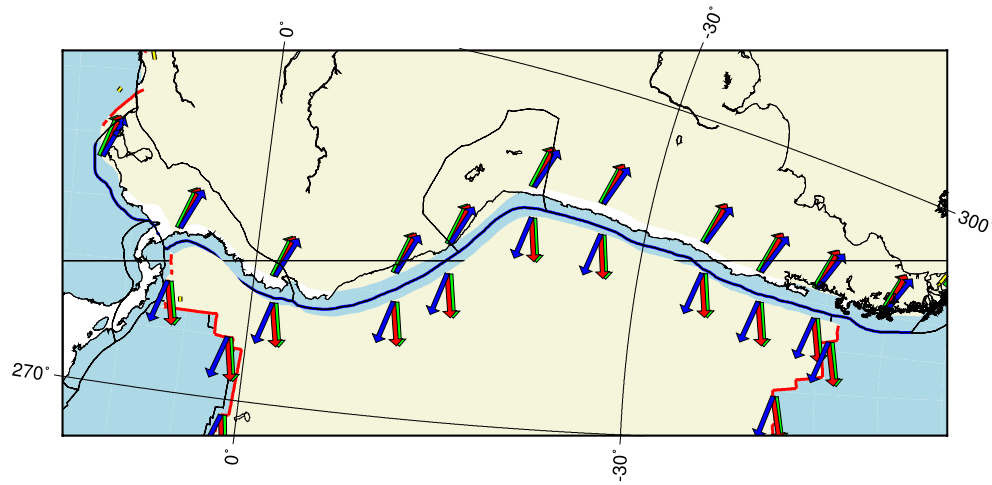

Figure 3. Orientations of required forces acting on the boundaries of the Nazca and South American plates. As for Figure 2, except that green and red arrows are calculated for Newtonian asthenosphere, with motions in the Nubian reference frame and the no-net-rotation reference frame of Argus et al. (2011), respectively. The green arrows have been shifted slightly to make them visible.

clumped isotope paleothermometer, Δ_{47} (e.g., Eiler, 2007), and (b) geologic observations that can be interpreted as resulting from elevation change, such as onsets of tectonic events or changes in erosion or incision rates. As we now discuss, those two lines of evidence taken together suggest a 2–3 km increase in mean elevation of the Central Andes, including the Altiplano, since ∼10 Ma, but also allow changes elsewhere at different times. Changes over the past 10–15 Ma both in $\delta^{18}O$ values from carbonate sediment (Garzione et al., 2006, 2008) and from fossil teeth (Bershaw et al., 2010) and in Δ_{47} values (Ghosh et al., 2006) suggest ∼2.5 km of surface uplift of the northern Altiplano (17–18°S) during the interval 11–10 and 7–6 Ma. Both $\delta^{18}O$ values and Δ_{47} values from southern Peru (15°S) suggest comparable elevation changes between ∼9 and 5.4 Ma (Kar et al., 2016), as does a study of paleobotanical finds (Martínez et al., 2020). Similar analyses for the southern Altiplano, 20–22°S, suggest a somewhat earlier rise of ∼2 km between 16 and 13 Ma and then ∼0.7 km between 13 and 9 Ma (Garzione et al., 2014) Also analyses of leaf physiognomy from sites in Bolivia suggest warmer conditions and lower elevations than today before ∼11 Ma (Gregory-Wodzicki, 2002; Gregory-Wodzicki et al., 1998).

Geomorphic evidence showing rapid incision of gentle surfaces that are now high concurs with, if does not suggest directly, abrupt surface uplift of the Central Andes near 12–10 Ma (e.g., Barke & Lamb, 2006; Gillis et al., 2006; Gubbels et al., 1993; Kennan et al., 1997). In addition, many studies suggest that beginning near 10 Ma, the locus of active deformation between ∼11°S and 23°S migrated eastward from the Eastern Cordillera to the Sub-Andes (e.g., Echavarria et al., 2003; Elger et al., 2005; Espurt et al., 2011; Gautheron et al., 2013; Hérail et al., 1996; Hoke & Garzione, 2008; Kley, 1996; Kley et al., 1997; Lease et al., 2016; Scheuber et al., 2006). Similarly, several studies suggest a tilting and incision of the west slope of the Central Andes at ∼10 Ma (e.g., Farías et al., 2005; Garcia & Hérail, 2005; Hoke et al., 2007; Jordan et al., 2010; Schildgen et al., 2007, 2009). In the southern part of the Puna, a switch from contraction to normal faulting at around 7 Ma suggests a change from crustal shortening to extension as would occur if mantle lithosphere were removed (Schoenbohm & Carrapa, 2015; Schoenbohm & Strecker, 2009).

The clearest evidence for surface uplift in this time interval north or south the central Andes comes from Ecuador. Hungerbühler et al. (2002) and Steinmann et al. (1999) showed ∼3 km of surface uplift of the western margin of the Andes (2–4.3°S) at ∼10 Ma. Spikings et al. (2010) reported thermo-chronological evidence based on fission tracks and [U-Th]/He data, which they interpreted as reflecting increased rates of erosion associated with uplift of the eastern Andes in three pulses between 15 Ma and the present. They attributed this rise to subduction of the Carnegie Ridge beneath the west coast of Ecuador, a possibility also considered by Hungerbühler et al. (2002) for the uplift of the western margin further south.

Ecuador aside, evidence for significant surface uplift of the Andes in the interval ∼10−6 Ma and outside the latitude range of ∼8–22°S is ambiguous or absent. Moreno et al. (2020) concluded that configuration of the

northernmost Peruvian Andes remained stable throughout this time interval, and Eude et al. (2015) interpreted their thermo-chronological and structural data as showing a post-(∼8)-Ma decrease in shortening rates across the eastern Andes at 5–7°S. Quade et al. (2015) argued for little late-Miocene change in elevation of the Andes of 22–26°S. In western Argentina at 30°S Jordan et al. (1993) show fairly continuous shortening on the west slope of the Andes over the past ∼15 Myr; although their preferred interpretation (Jordan et al., 1993, Figure 14) shows a peak in shortening rate at about 10 Ma, the geochronological uncertainties are large enough to encompass a constant rate. In Argentina at 31–33°S, Levina et al. (2014) and Mackaman-Lofland et al. (2020) reported a relatively steady migration of the locus of deformation since 24 Ma, but they also found a pulse of exhumation at 13–10 Ma that suggests accelerated deformation then. Similarly, Farías et al. (2008) reported a brief period of stream incision, some time between 10 and 4 Ma, in Chile at 33–35°S from which they inferred surface uplift.

Collectively, these studies suggest a major phase of surface uplift of the central Andes between 10 and 6 Ma. Several lines of evidence suggest that in some places this process started, or perhaps took place, earlier. As examples, a phase of surface uplift is recorded in the southern part of the Central Andes starting as early as 16–13 Ma (Garzione et al., 2014), Thouret et al. (2007) argued that tilting of the western side of the Andes began at ∼13 Ma, before accelerating at 9 Ma, and Schoenbohm and Carrapa (2015) report a transition from contraction to extension at 17–16 Ma. In other places, the uplift may have started later; for example, in central Peru (8.5–11°S), both rapid cooling implying accelerated exhumation (Garver et al., 2005; Margirier et al., 2016) and dating of lavas in the adjacent basin (Giovanni et al., 2010) suggest that normal faulting in the Cordillera Blanca began at 5–6 Ma.

Quiero et al. (2022) presented a model that links multiple decelerations and accelerations of Nazca-South America convergence to changes in horizontal shortening, and to intrusive and extrusive igneous activity, within western South America; the only quantitative assessment we can make of these scenarios concerns the history of surface elevation, which we have discussed above.

3.3. Mechanical Implications

The hypothesis that rise of the Andes slowed convergence between the Nazca and South American plates (e. g., Garzione et al., 2006, Iaffaldano et al., 2006, Norabuena et al., 1999) passes a quantitative test by accounting for the post-12 Ma changes in angular velocity of both Nazca and South America in terms of a single resisting force acting approximately perpendicular to their shared boundary (Section 3.1, Figures 2 and 3).

Other explanations for the slow-down have, however, been advanced. Breaking off of slabs is a popular explanation for a multitude of geological observations (see Garzanti et al., 2018, for a review), and has been invoked to explain several aspects of Andean tectonics (e.g., Haschke et al., 2006). That process does not appeal in the present context, first because a shortening of the length of slab pulling the plate would be accompanied by a decrease in the resistance along the sinking slab; it is therefore not clear whether the breaking off of a slab would decrease the net slab pull. Moreover, although the removal of negative buoyancy from the Nazca plate might slow its motion, it provides no explanation for the simultaneous change, of similar magnitude and orientation, in force on the South American plate (Table 1, Figure 3). This objection does not apply to the suggestion of Martinod et al. (2010) that slowing of the Nazca plate could have resulted from the onset of sub-horizontal subduction beneath Peru and North-Central Chile, nor to the suggestion of Martinod et al. (2020) that the increase in elevation of the Central Andes could have resulted from the slab's steepening from sub-horizontal to its present dip, with replacement of cool lower lithosphere by hotter asthenosphere.

In the absence of a rule that gives the resisting force due to flat-slab subduction, we cannot analyze the suggestion of Martinod et al. (2010), but the suggestion of Martinod et al. (2020) shares with those of Garzione et al. (2006), Iaffaldano et al. (2006), Norabuena et al. (1999) an increased GPE of the mountain range, and those suggestions can be evaluated, because changes in GPE provide a scale for measuring the forces involved in the changes in motion (Appendix B).

We adopt as a lower bound on the along-strike extent of the increase in surface height the latitude range of 12–22°S, or 1,100 km, from which most of the indicators of uplift at this time come. This extent could be increased by about 450 km if the structural evidence of transition to extension in the southern Puna (Schoenbohm & Carrapa, 2015; Schoenbohm & Strecker, 2009) were taken to indicate surface uplift at this time, although such uplift appears inconsistent with paleoisotopic data (Quade et al., 2015, and references therein). A similar increase

in extent could be implied by the evidence of uplift in northern Peru (to approximately 8°S). The uplift in Ecuador, part of which is coeval with the uplift we study here, was likely associated with the subduction of the Carnegie Ridge and, although this may also have increased resistance at the convergent plate boundary (Section 2.1), we do not include it in our force balance.

We therefore let the length of boundary associated with the uplift between ~12 and ~6 Ma be 1,000 km. Many of the indicators of uplift suggest an elevation increase of $\gtrsim$2 km. Such elevation changes are unlikely to result from convective removal of mantle lithosphere alone (Appendix B), but are readily explained if substantial removal of mantle lithosphere is accompanied, or followed by, loss of eclogitic lower crust, as suggested by Jull and Kelemen (2001) and Kay and Mahlburg Kay (1991). Using Figure B2, we estimate that the change in GPE is likely to have been in the range ~4–8 TN m^{-1}; so $\Delta F_b \approx 6 \pm 2 \times 10^{18}$ N.

The change in dimensionless torque calculated for the change in speed of the Nazca plate for a Newtonian substrate is 3.7×10^{-3}, and for South America it is 2.5×10^{-3}. The coefficient of basal drag, B_0/D, Equation 21, is 2×10^{14} Pa s m^{-1} for the Nazca plate, and for the South American plate it is 2.9×10^{14} Pa s m^{-1} (Table 1). With $D \sim 40$ km we estimate the viscosity, B_0, at the base of the Nazca plate to be $\eta \sim 8 \times 10^{18}$ Pa s, and $\eta \sim 1.2 \times 10^{19}$ Pa s for the base of the South American plate. For the case of non-Newtonian asthenosphere, we must specify a reference frame (Equation 15), which we first choose to be the Nubian plate. With $n = 3.5$, $B_0/D^{1/n}$ Equation 21, is 3.2×10^8 Pa (s/m)$^{1/3.5}$ for the Nazca plate, and for the South American plate it is 4.3×10^8 Pa (s/m)$^{1/3.5}$. If the frame of reference is chosen to be the NNR-MORVEL frame (Argus et al., 2011), the constant of proportionality becomes 1.3×10^8 Pa (s/m)$^{1/3.5}$ for the Nazca plate, and 5.7×10^8 Pa (s/m)$^{1/3.5}$ for the South American plate. The uncertainties in these estimates of drag coefficient are discussed in Section 5.1 and their implications are discussed in Section 5.2.

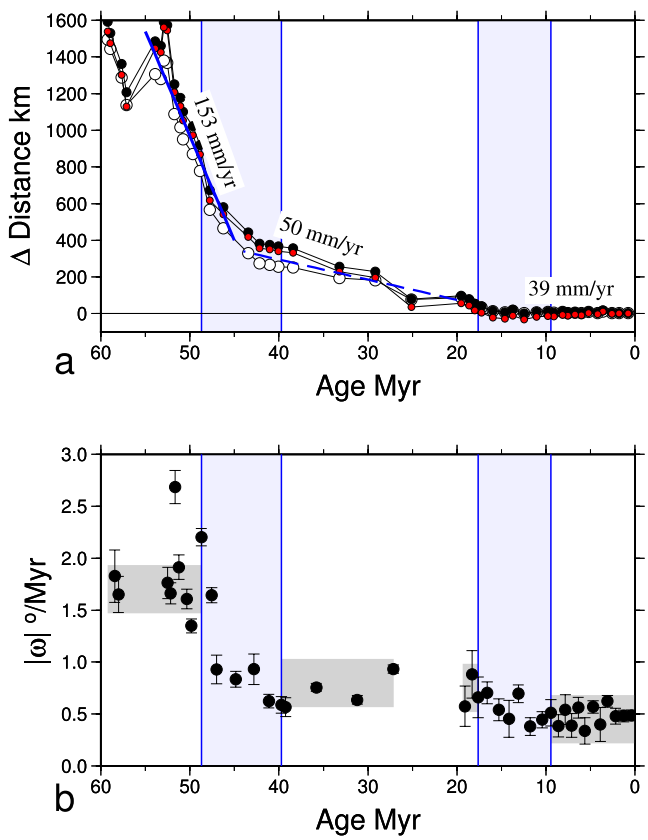

Figure 4. Variations in time of position and angular velocity of the Indian plate. (a) Distances from their current positions of three points (Points 4, 5, and 6 in Figure 5) on the IN-EU plate boundary; the distances are reduced by 33, 39, and 47 mm/yr for respectively, the open (Point 4), black (Point 5), and red (Point 6) circles. Finite rotations are from DeMets and Merkouriev (2021). (b) Variation in magnitude of stage angular velocities between 60 Ma and present, calculated from the finite rotations of DeMets and Merkouriev (2021) as described in the text. Gray bands show the time intervals over which angular velocities are averaged to calculate the difference in torques (Figure 5).

4. Cenozoic Changes in India-Eurasia Relative Motion

Reconstructions of the relative positions of the India and Eurasia plates consistently indicate a slowdown in convergence rates between 50 and 40 Ma (e.g., DeMets & Merkouriev, 2021; Dewey et al., 1989; Molnar & Stock, 2009; Molnar & Tapponnier, 1975; Patriat & Achache, 1984). Additionally, Molnar and Stock (2009) reported a reduction in the rate of convergence between India and Eurasia between about 20 and 10 Ma, and DeMets et al. (2020) argued for an approximately 50% reduction in convergence rate between 20 and 12 Ma. Figure 4a shows displacements of points on the northern margin of the present-day Indian plate, calculated for the past 60 Myr from the finite rotations of DeMets and Merkouriev (2021). They confirm two sharp decreases in the convergence rate, one from >150 to ~50 mm/yr between ~48 and 41 Ma and one from about 50 mm/yr to about 40 mm/yr starting some time after about 25 Ma and ending at or before 10 Ma. Similarly, the stage angular velocities of DeMets and Merkouriev (2021) exhibit three phases: pre-50 Ma their magnitudes are 1.5°/Myr or higher; between about 48 and 41 Ma the rates decrease to ~0.7°/Myr; between about 25 and 12 Ma the rates decrease to ~0.45°/Myr (Figure 4b).

The earlier of these slowdowns is generally attributed to processes associated with contact between the Indian and Asian continental lithospheres. The suggestion of Molnar and Stock (2009) that the slowdown in Miocene time may reflect an increase in GPE of the Tibetan plateau is less secure, and it remains to be demonstrated that the forces leading to that slowdown acted at the northern edge of the Indian continent.

Relative motion between the Capricorn and Indian plates was slow before about 8 Ma (DeMets et al., 2005), so we use a combined Indian-Capricorn

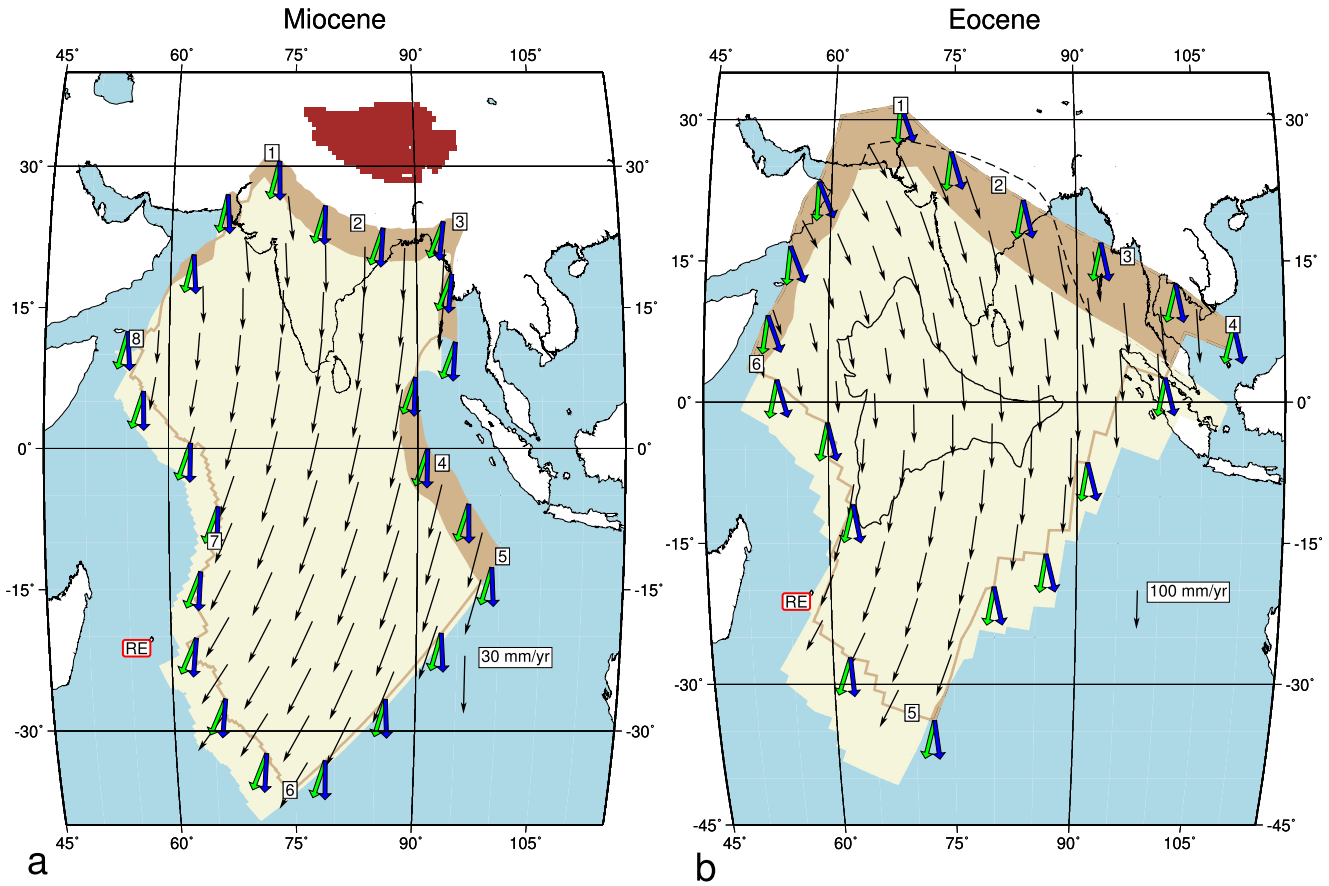

Figure 5. (a) Change in motion of the Indian-Capricorn plate between 20 and 10 Ma (DeMets & Merkouriev, 2021); positions of the plate immediately before and immediately after the change are shown, respectively, by beige and tan polygons. Blue arrows show the orientation of the force which, if acting alone on the relevant segment of boundary, would produce the change in torque (Equation 19), calculated for a non-Newtonian asthenosphere (lines labeled $n = 3.5$, EU in Table 1); green arrows are for the Newtonian case. Maroon shading shows the areas in Tibet where surface height exceeds 4,750 m. (b) As (a) for changes between 48 and 43 Ma. Extent of the Indian plate at 50 Ma is from Torsvik et al. (2010), except for the exclusion of a small area outlined by the dashes (see text). The position of present-day continental India at 50 Ma is shown in black outline. The label RE marks the location of the Réunion hotspot.

plate for our calculations of torque changes between 20 and 10 Ma (Figure 5a). Although oceanic lithosphere has been added to these plates since 20 to 10 Ma, and some continental area has been lost at the north of India, we do not attempt to correct for those changes, which represent a small fraction of the total plate area. For the shape of the plate in Eocene time, we modify the version of the Indian plate for that time given by Torsvik et al. (2010) to exclude a small part of "Greater India" that seems, to us, to be implausible (Figure 5b); this exclusion has negligible influence on our calculations.

To represent the change in motion between ~20 and 10 Ma, we averaged the stage angular velocities derived from finite rotations of anomalies 6no–5Dy (19.535–17.235 Ma), and those from anomalies 5n.1–1no (9.786–0.773 Ma) (DeMets & Merkouriev, 2021, Table S5 in Supporting Information S1, and see Figure 4b). For the Eocene change in motion, we averaged angular velocities derived from anomalies 26no to 21n.1o (59.2–47.8 Ma), and those from anomalies 19ny to 8n.1y (41.0–25.1 Ma) (DeMets & Merkouriev, 2021, Table 1 and see Figure 4b); we omitted angular velocities derived from anomalies 6AAr2n to 24n.3o, for the reasons given in Appendix A2. The associated changes in velocity are shown in Figure 5. The orientations of the changes in force, $\mathbf{\Delta F}_b$, that would be required at individual segments of a boundary if a change at that segment alone were to balance the change in torque (Equation 19) are shown as blue arrows for a non-Newtonian asthenosphere, and as green arrows for a Newtonian asthenosphere.

To consider the forces that could be responsible for the slowdowns of India we use the same system of argument as for Nazca and South America. The required boundary forces for the Miocene slowdown are shown in Figure 5a. Forces on the eastern edge (segment 6 to 3) and western edge (segment 6 to 8) of the plate correspond

to decreases in left-lateral shear (east) and right-lateral shear (west). These would correspond to an increase (not decrease) in northward rate of motion, or to a sudden increase in strength of the material near the boundary, which is implausible. The required change in force on the Capricorn-Australian plate boundary (segment 5 to 6) corresponds to a combination of reduced compressional force and increased right-lateral shear, which is hard to explain. In contrast, the required forces on the northern boundary (segment 1 to 3) act approximately perpendicular to the boundary, as would be expected for an increase in GPE behind it. The arguments for the Eocene slowdown parallel those for the Miocene, and arrive at the unsurprising conclusion that the forces responsible acted approximately normal to the northern margin of the Indian plate (segment 1 to 4, Figure 5b).

4.1. Changes in Driving and Resisting Forces During India-Eurasia Convergence

4.1.1. Miocene Changes in GPE of Tibet

We presume, as for example, did England and Houseman (1988, 1989), Molnar et al. (1993), and Molnar and Stock (2009), that convective removal of mantle lithosphere in Miocene time increased the GPE of parts of Tibet, leading to increased resistance to convergence between India and Eurasia. Many proxies for surface elevation have been obtained from the Tibetan plateau over the past couple of decades, with uncertainties in the estimates of height being typically of order a kilometer (see Molnar, 2022, and references therein). As Figure B2a shows, the likely full range of GPE changes associated with convective removal of the lower lithosphere is accompanied by surface height changes of 1.5 km or less. We therefore concentrate on the transition between crustal thickening and normal faulting, which is diagnostic of change in GPE (e.g., England & Houseman, 1989; Molnar et al., 1993; Platt & England, 1994).

Structural observations across the Jangtang suggest crustal shortening as large as 50%, during Cretaceous time (Kapp et al., 2003, 2005, Kapp, DeCelles, Leier, et al., 2007; Li et al., 2011, 2012; Volkmer et al., 2007, 2014; Wu et al., 2012). Shortening continued into Cenozoic time, with the last thrust faulting dated at ~20–25 Ma (Kapp, DeCelles, Gehrels, et al., 2007; Kapp et al., 2003). North of the Jangtang, coarse sediment, derived from the south (presumably from the Jangtang) accumulated over a wide region in the Hoh Xil Basin until ~50 Ma (Leeder et al., 1988; Li et al., 2018; Staisch et al., 2014; Wang et al., 2008). Subsequent thrust faulting and folding accommodated ~25% shortening of the region but flat overlying basalt flows demonstrate that this shortening had stopped by 27 Ma (Staisch et al., 2016). Gentle folding of overlying sedimentary rock implies negligible subsequent shortening (Staisch et al., 2016; Wang et al., 2002, 2008; Wu et al., 2008). Normal faulting was established in the interior of the plateau by ~15 Ma (Blisniuk et al., 2001; Harrison et al., 1995; McCallister et al., 2014; Pan & Kidd, 1992; Styron et al., 2013; Wolff et al., 2019; Woodruff et al., 2013); because constraints on the timing of this faulting come generally from radiometric cooling ages, it is possible that it began earlier than 15 Ma. The interval between the end of compression and well-established extension corresponds to the interval of decreasing angular velocity of India with respect to Asia (Figure 4b) associated with increased resistance on the northern margin of India (Figure 5d).

Horizontal dilatation and crustal thinning within the Tibetan plateau are restricted to places where the surface height exceeds 4,750 m (Elliott et al., 2010; Molnar et al., 1993). The E-W extent of this region is about 1,400 km (Figure 5b), and the average surface height within it is 5,000 m. One way to estimate change in GPE might be to assume that the elevation change accompanying extension was only 250 m–equivalent to a change in driving force of 1 TN m^{-1} (Figure B2a), and $\Delta F_b \sim 1.5 \times 10^{18}$ N. However, the crust of the plateau is currently thinning at about 10 nano-strain per year (Ge et al., 2015), so would have been about 10% thicker when extension began, with its average surface height close to 6 km. That scenario would imply an increase in GPE of up to 5 TN m^{-1} and $\Delta F_b \sim 7 \times 10^{18}$ N, and higher if loss of eclogitic lower crust occurred (Figure B2b). We proceed with an estimate of $\Delta F_b \sim 4 \pm 3 \times 10^{18}$ N.

The value of the dimensionless change in torque, $\Delta T_p'$, during the Miocene slowdown is 1.9×10^{-3} for Newtonian asthenosphere (Table 1); this gives $B_0/D \sim 2.5 \times 10^{14}$ Pa s m^{-1}, hence an estimate of $\sim 10^{19}$ Pa s for the viscosity immediately beneath the plate, for $D \sim 40$ km. In the non-Newtonian case, the estimate of $B_0/D^{1/n} \approx 4 \times 10^8$ Pa $(s/m)^{1/3.5}$ is in the middle of the range of $B_0/D^{1/n}$ estimated for the Nazca and South American plates (Table 1).

4.1.2. Contact of India With Asia

A wide range of timings has been proposed for what is commonly referred to as the "collision" between India and Asia. The rapid change in angular velocity of the Indian plate between about 48 and 41 Ma (DeMets & Merkouriev, 2021)

requires a marked increase in the resisting force (or decrease in the driving force), acting at the north of continental India (Section 4), and this interval therefore encompasses the major change in dynamics of the Indian plate during Cenozoic time. That this change should have taken a few million years is consistent with the likelihood that the northern margin of the India plate did not meet flush with the southern margin of Eurasia, so that the transition from a subduction boundary at the north of India to contact between two continents would have been gradual. Other arguments about when full contact between the two continental masses occurred, such as absence of marine rocks in parts of the suture zone, or estimates of the northern extent of India, seem less secure. We therefore proceed with the assumption that a major change in the forces acting on the Indian plate occurred between about 48 and 41 Ma.

4.1.3. Change in Force Balance During Eocene Slowdown of India

It reasonable to assume that the physical properties of the asthenosphere beneath the plate during the Eocene change in motion should have been similar to those during the Miocene change, hence that the coefficient of drag, $B_0/D^{1/n}$, was similar. The change in dimensionless torque for Newtonian asthenosphere was $\sim 9 \times 10^{-3}$ which corresponds to an increase in resisting force, ΔF_B, $\sim 10^{19}$ N (Table 1), and the same value (to one significant figure) is found for non-Newtonian asthenosphere. van Hinsbergen et al. (2011) investigated the suggestion that waning influence of the Réunion hotspot may have contributed to the reduction in India's velocity, but concluded that this process was likely to have been weak in comparison with changes at the northern margin of the plate. So, we concentrate on the latter changes.

The length of the northern edge of the Indian plate was about 5,000 km (Figure 5d); if the increase in resisting force were distributed evenly along the boundary, it would have been equivalent to ~ 2 TN m^{-1}. Although the shape of the Indian plate changed between Eocene and Miocene time, it is reasonable to assume that the length of the continent-continent boundary was approximately the same then as it is now (~2,500 km), so we may, alternatively, calculate that an increased resistance of ~ 4 TN m^{-1} was concentrated along that section of the boundary.

It has been argued that the cause of the increased resistance was the growth in thickness of the Tibetan crust (e.g., Copley et al., 2010). This explanation for the abrupt slowdown is inconsistent with the protracted history of crustal thickening in Tibet, referenced above, which occurred both before and after the Eocene slowdown (see also van Hinsbergen et al., 2011). Furthermore, it seems probable that an Andean-type margin followed the southern edge of Eurasia during latest Mesozoic and early Cenozoic time (e.g., England & Searle, 1986; Gansser, 1980; Kapp, DeCelles, Leier, et al., 2007; Yakovlev & Clark, 2014), and therefore that much of the Transhimalaya of southern Tibet had already reached an elevation of several kilometers, perhaps as high as the present day (~4,500 m), before contact between the continents took place (see also Molnar, 2022, and references therein). Although crustal thickening did take place post-48 Ma, it would not have led to an important increase in the resisting force until a significant part of the plateau attained a GPE that was greater than that of the Transhimalaya (e.g., Section 4.1.1).

Clark (2012) suggested that the work required to deform Asia, rather than to increase its GPE, could contribute to the resisting force. Although the details of that suggestion, which involved exponential decay in convergence rate since contact between India and Asia, are not borne out by the recent reconstructions (DeMets et al., 2020; DeMets & Merkouriev, 2021), we cannot rule out some contribution to increased resistance between ~48 and 41 Ma from the work required to deform the interior of Asia (see Section 5.1).

It may also be the case that a rapid decrease in driving force resulted from the subduction of (perhaps thinned) continental crust attached to the northern margin of the Indian plate, but the constraints on the force required for this process are loose (e.g., Molnar & Gray, 1979).

We may place a bound on the net driving force per unit length on the subducting oceanic lithosphere of the Indian plate before ~48 Ma by assuming that the subsequent change in force balance was entirely due to the loss of slab from the north of the Indian plate. If that loss were from 2,500 km of plate boundary (the present width of the Himalayan front), then its net driving force must have been lower than ~ 4 TN m^{-1}; if slab was lost from the whole 5,000 km width of the northern boundary to the Indian plate, then its net driving force was lower than ~ 2 TN m^{-1}. This accounting implies that the net driving force was small in comparison with the likely negative buoyancy of the slab–in turn implying, as previous global studies have suggested, that this buoyancy is to a large extent compensated by resisting forces at convergent boundaries (e.g., Backus et al., 1981; Chapple & Tullis, 1977; Forsyth & Uyeda, 1975; Hager & O'Connell, 1981).

5. Discussion

5.1. Uncertainties

The principal uncertainties in our calculations are epistemic, and therefore hard to quantify. The leading assumption, that changes in basal drag act anti-parallel to changes in velocity, may introduce biases. Comparison of the torque changes for Nazca and South America calculated in the Nubian and NNR frames (Table 1, and Figure 2) shows that this bias may lead to uncertainties in orientation of the boundary forces of order 10°. Additionally, orientations of those forces vary by 10–20° depending on the assumed rheology of the asthenosphere (Figures 3 and 5). Those uncertainties in orientation are small enough, however, that they do not affect our attribution of the forces causing abrupt changes in plate motion to increased resistance at the convergent boundaries (Sections 3.1 and 4, and Figures 2, 3 and 5). The major plate reorganization accompanying the slowdown of India in Eocene time may render our leading assumption invalid, and uncertainties in the orientation and magnitude of the accompanying change in torque are larger than those for the other changes we consider. For this reason, we do not rely on the details of torques and forces in Figure 5d.

Changes in basal traction are given by changes in resistance at the convergent boundaries, divided by the plate area (Equation 22 and Table 1). Our estimates of the former are uncertain by approximately 50% (Sections 3.2, 4.1.1 and 4.1.3, and Appendix B). An additional uncertainty is attached to the inclusion of the Capricorn plate with India in the calculations for the Miocene slowdown; its exclusion would double the magnitude of the change in basal traction.

The coefficient of drag, $B_0/D^{1/n}$, is calculated from the dimensionless torque change (Equation 21), and from the GPE changes associated with mountain uplift. Inspection of Figures 1 and 4 suggests that magnitudes of the average angular velocities used in calculating torques before and after major changes in plate motion are uncertain by ∼10%–20%. We therefore place an uncertainty of ∼30% on changes in the magnitudes of torques. We have estimated the changes in boundary forces from the changes in GPE of the adjacent mountain belts. Those changes are supported in part by changes in deviatoric stress within the mountain belts (Section 2.1). We may estimate the magnitude of such support by considering the forces required to deform the present-day Tibetan Plateau. The effective viscosity of the Tibetan lithosphere is estimated to be in the range 0.5–5 × 10^{22} Pa s, averaged over a nominal lithospheric thickness of 100 km (e.g., Flesch et al., 2001; Vergnolle et al., 2007). The present-day shortening strain rate within the plateau is ∼3 × 10^{-16} s^{-1} (Ge et al., 2015), hence the associated average deviatoric stress is 1.5–15 MPa which, for 100 km of lithosphere, is equivalent to a force per unit length 0.15 to 1.5 TN m^{-1} (This range is unaffected by the thickness assumed for the lithosphere because the estimated viscosity is inversely proportional to that thickness.) Taking an uncertainty of ∼1 TN m^{-1} together with the uncertainties in the boundary force change, ΔF_b, we estimate that the coefficient of drag is uncertain by a factor of approximately two.

5.2. Basal Drag Coefficient

Our estimates of basal drag coefficient are between 2 and 3 × 10^{14} Pa s/m for a Newtonian asthenosphere, and between 1 and 6 × 10^8 Pa $(s/m)^{1/3.5}$ for non-Newtonian asthenosphere with $n = 3.5$ (Table 1). Forsyth and Uyeda (1975) used a global kinematic model to solve for the relative magnitudes of the forces driving and resisting plate motion, then calibrated the basal tractions against the ridge push, obtaining a coefficient of drag equal to 6.25 × 10^{-3} MPa of traction per mm/yr of velocity relative to the deep mantle (Forsyth & Uyeda, 1975, p. 194). This quantity is equivalent to B_0/D = 2 × 10^{14} Pa s/m (Equation 10), very close to our estimates for Newtonian asthenosphere, calibrated against changes in GPE of mountain ranges.

Forsyth and Uyeda (1975) also found the coefficient of drag beneath continental lithosphere to be seven times stronger than beneath the oceans. Chapple and Tullis (1977) found no drag on the bottom of oceanic plates to be needed, and only a small drag at the base of continental lithosphere. Hager and O'Connell (1981) calculated the force balances on plates from a global dynamical model in which flow in the mantle was driven by the density variations associated with thickening of oceanic lithosphere and with the subducting slabs. Using asthenospheric viscosity of 4 × 10^{19} Pa s, they found basal tractions of order 0.1–1 MPa, comparable to those we find here. Conrad and Lithgow-Bertelloni (2006) used a global model with density variation inferred from seismic tomography, and found basal tractions of a few MPa for an asthenospheric viscosity of 10^{20} Pa s.

Table 2
Average Basal Shear Tractions on Plates, Calculated From Their Velocities in the NNR-MORVEL Reference Frame Argus et al. (2011) (Equation 10)

	$\overline{\sigma}$ (MPa)	
Plate	$n = 1$	$n = 3.5$
Antarctica	0.11	0.67
Arabia	0.28	0.90
Australia	0.38	0.98
Caribbean	0.09	0.65
Cocos	0.47	1.04
Eurasia	0.09	0.64
India	0.34	0.95
Juan de Fuca	0.10	0.67
Nazca	0.43	1.01
North America	0.11	0.69
Nubia	0.09	0.64
Pacific	0.39	0.99
Somalia	0.19	0.80
South America	0.06	0.59

If we assume that the drag beneath oceanic lithosphere is everywhere the same, then we may estimate the relative drag coefficient, B_C, for the continental portions of the Indian and South American plates from the ratio of their $B_0/D^{1/n}$ to that of the entirely oceanic Nazca plate. Using superscript NZ to denote the Nazca plate

$$\frac{B_0/D^{1/n}}{B_0^{NZ}/D^{1/n}} = B' = 1 + \chi\,(B_C - 1) \tag{23}$$

$$B_C = \frac{B' + \chi - 1}{\chi} \tag{24}$$

where χ is the fraction of the plate's surface area that is continental: 0.2 and 0.4, respectively, for India and South America. For Newtonian (non-Newtonian) asthenosphere, B' for Miocene India is 1.3 (1.2) and for South America it is 1.5 (1.4); ratios are calculated, in the non-Newtonian case, using the Nubian and Eurasian reference frames. Equation 24 gives estimates of the basal drag beneath continents of 2–3 times that beneath oceans. This ratio is close to that calculated by Conrad and Lithgow-Bertelloni (2006) from their models of global flow.

It is of interest to calculate basal tractions on other major plates using the rheological parameters we have determined here. Table 2 shows average tractions on the major plates, calculated from their velocities in the NNR-MORVEL reference frame (Argus et al., 2011); we use the coefficients of drag obtained for the Nazca plate in the NU reference frame: $B_0/D = 1.9 \times 10^{14}$ Pa s/m in the Newtonian case and $B_0/D^{1/n} = 3 \times 10^8$ Pa $(\text{s/m})^{1/3.5}$ for non-Newtonian asthenosphere. If the asthenosphere is assumed to be Newtonian, average shear tractions are between 0.1 and 0.5 MPa; for non-Newtonian asthenosphere, they are between 0.6 and 1 MPa. All of these tractions must be considered uncertain by approximately a factor of two because of uncertainty in the changes in driving force, ΔF_b which relates torque changes to the rheological parameter (Equation 21), and because of variation with choice of reference frame (which can be seen as variation in torque for Nazca and South America in Table 1). Nevertheless, as noted by Hager and O'Connell (1981), basal tractions of this magnitude exert resisting forces on plates that may be comparable in magnitude to the driving forces arising from aging of the oceanic plates.

6. Conclusions

High-resolution reconstructions of plate motion of DeMets and Merkouriev (2019, 2021) allow sharper focus on the relations between changes in plate motion and rapid rises in mountain ranges, and enable diagnosis of which boundary forces can plausibly be related to the change in basal drag (Section 2). The changes in torque due to basal drag on the Nazca and South American plates during their slowdown in late Miocene time cannot be explained by forces arising from hotspots. Nor can they be reconciled with any change in boundary force other than increased resistance on the convergent boundaries of each plate (Section 3.1, Figure 2). Geological observations and data show that, at the same time, the surface of the central Andes rose by ~2 km or more, which would have generated an increase in GPE–hence in resistance to convergence–of ~4–8 TN m^{-1} (Section 3.2). Similarly, the only change in boundary forces that could plausibly have balanced the changes in basal drag associated with the Miocene slowdown of India correspond to increased resistance on the north of continental India (Section 4, Figure 5), and that slowdown coincided temporally with an increase in GPE of the Tibetan plateau (Section 4.1.1).

Whereas the decrease in Nazca-South America convergence might have resulted from a transition to sub-horizontal subduction of part of the slab (Martinod et al., 2010), a similar explanation is not available for the Miocene slowdown of India. These two independent demonstrations that the forces required to account for the change in angular velocities of the plates act at their convergent boundaries (Figures 2 and 5) support the hypothesis that rapid changes in the GPE of mountain ranges cause comparably rapid changes in plate motion (e.g., Garzione

et al., 2006; Heidbach et al., 2008; Iaffaldano et al., 2006; Molnar & Stock, 2009; Norabuena et al., 1999). Our analysis, which is encapsulated in Figures 1–5 depends only on simple force balances on rigid shells.

The principal change in dynamics of the Indian plate in early-Cenozoic time accompanied the slowdown in the convergence of India with Eurasia, between about 48 and 41 Ma. Although, as discussed in Section 5, uncertainties in our estimates of changes in force for the Eocene slow-down are greater than for the other cases, our analysis places an upper bound of 2–4 TN m^{-1} on the change in boundary force associated with the loss of subducting slab at the north of the Indian plate (Section 4.1.3); if additional resisting forces were required to deform Asia, or to subduct continental crust, the net force per unit length associated with subducting slab would be correspondingly reduced. This conclusion supports previous demonstrations, from global dynamic and kinematic models of driving forces (Backus et al., 1981; Chapple & Tullis, 1977; Forsyth & Uyeda, 1975; Hager & O'Connell, 1981; Lithgow-Bertelloni & Richards, 1995), that the negative buoyancy of slabs is close to being balanced by forces resisting their descent into the mantle.

The changes in torque associated with rapid mountain uplift allow us to calculate basal drag coefficients for the individual plates (Table 1) without the uncertainties attached, in global models, to the small differences between the large driving and resisting forces at subduction zones (Section 2.2). These coefficients give estimates of basal shear tractions of the order of 0.1–1 MPa, at which level they make a contribution to the force balance on the plates that is comparable in magnitude with, but counteracting, the forces associated with thickening of the oceanic lithosphere (Hager & O'Connell, 1981).

Appendix A: Finite Rotations

A1. Nazca-Nubia Finite Rotations

We calculated the relative motions between the Nazca and Nubian plate from the Nazca-South America reconstructions of Garzione et al. (2006) (Table A1) and the Nubia-South America reconstructions of DeMets and Merkouriev (2019). We excluded from the former set the reconstruction for anomaly 5. As can be seen from Figure 1, this reconstruction is inconsistent with those either side of it. The inconsistency probably arises from the use of data from the Chile Ridge, whose spreading underwent complex reorganization around this time (Tebbens

Table A1
Nazca-South America Finite Rotations of Garzione et al. (2006)

Anomaly	Age (Ma)	Lat ºN	Lon ºE	Ω
2	1.860	56.23	−98.97	−1.227
2A	2.581	56.81	−97.38	−1.754
3	4.710	56.40	−95.98	−2.872
3A	6.203	54.34	−91.99	−4.145
4	7.861	52.96	−91.19	−5.954
4A	8.862	52.95	−89.85	−7.219
(*5*	*10.435*	*52.38*	*−89.64*	*−9.682*)
5A	12.168	51.85	−87.93	−10.994
5B	14.961	55.22	−90.58	−13.955
5C	16.395	56.28	−92.10	−15.499
5D	17.446	57.40	−92.47	−16.929
5E	18.531	58.20	−93.22	−18.109
6	19.589	58.52	−93.94	−19.226
6A	20.919	59.79	−94.68	−21.774

Note. The plate circuits are described in Section 7.3 of Garzione et al. (2006) but the rotations are not listed. We exclude anomaly 5 from our analysis, as discussed in the text. Note that the ages assigned to the anomalies are those used in the original publication; They have not been corrected for subsequent recalibrations of the geomagnetic polarity timescale. Italicized values indicate that they are excluded from analysis.

et al., 1997). We calculated the angular velocities at each stage (except the earliest) from the differences between the stage poles either side of that time.

A2. Remarks on Finite Rotations and Stage Angular Velocities of DeMets and Merkouriev (2021)

In deriving a history of India's convergence with India, DeMets and Merkouriev (2021) reported a brief decrease in rate between ~25 and 22 Ma and then an increase between 22 and 18 Ma. Their calculated rate of convergence drops from 55 to 60 mm/yr between 43 and 24 Ma to ~35 mm/yr for an interval centered near 22 Ma, and then returns to 55–60 mm/yr between 19 and 17 Ma. For a variety of reasons, we question that abrupt drop in rate and then brief acceleration.

To reconstruct the plates in that period DeMets and Merkouriev (2021) must rely on an interpolation between 33 and 20 Ma for the North Atlantic and Arctic (DeMets & Merkouriev, 2021, Figure 23). Although average rates since ~20 Ma and between 39.5 and 33 Ma are comparable, between 33 and 20 Ma they were ~20% lower (Gaina et al., 2002). When changes in rates between 33 and 20 Ma occurred is poorly constrained.

Of greater concern is the history of spreading in the Central Atlantic between North America and Africa. First, uncertainties in reconstructions do not depend on rates but the geometry of the plate boundary (e.g., Chang, 1986; Stock & Molnar, 1983). In particular, the largest errors commonly arise for reconstructions based on a short length of a spreading center; the uncertainty can be described as a small perturbing rotation about the geometric centroid of the data used for such a reconstruction. Then, in reconstructing points on plates far away, a small error associated with that perturbation can grow to reach a maximum 90° away; the Central Atlantic lies ~90° from the India-Eurasia convergence zone. Imagine errors in magnetic anomaly crossings of 5 km, certainly not an unreasonable value, of opposite sign along a 2,000-km-long spreading center. The error would be an angle of arcsin (5 km/1,000 km) $\approx 5 \times 10^{-3}$ about the centroid. At a distance of 90° from that point, the error in position would grow to $R \times 5 \times 10^{-3} \approx 30$ km.

A further hint that this brief period is an aberration comes from differing reconstructions of the Central Atlantic in the period 33 to 20 Ma. DeMets and Merkouriev (2021) and Schettino and Macchiavelli (2016) reported poles and angles of rotation for different chrons in the period between 19.5 and 25 Ma (DeMets & Merkouriev, 2021, Figure S9 in Supporting Information S1). First, fits of synthetic to recorded magnetic anomalies in the interval 20–33 Ma, as shown in Schettino and Macchiavelli's (2016) Figure 14, allow for errors in positions of 5 km, if not 10 km or more. Second, identifications of anomaly 6B on the east flank are not many (Schettino & Macchiavelli, 2016, Figure 8). Most important, Schettino and Macchiavelli (2016, Figure 10) found that poles of finite rotation moved systematically eastward between 33 Ma and the present, except for a brief step back to the west between 22.59 (chron 6) and 21.69 Ma (chron 6B) (DeMets and Merkouriev, 2021). Given that chron six is the more easily identified, it seems logical that the aberration in what appears to be a steady, systematic pattern can be assigned to relatively sparse, inaccurate positions of magnetic anomaly 6B.

In summary, not only is there good reason to doubt the positions of anomaly 6B, but aleatoric uncertainties in their positions allow for large uncertainty in calculated positions of India with respect to Eurasia when the magnetic field reversed to produce this magnetic anomaly.

In addition, we exclude from our analysis two stage angular velocities obtained using anomaly 24n.3o; these span the interval 52.5 to 57 Ma, which DeMets et al. (2021) (their Figure 24 and discussion following) identify as being associated with artifacts arising from improbable shifts in their India–Somalia stage angular velocities at that time.

Appendix B: Change in Gravitational Potential Energy Associated With Convective Instabilities Beneath Mountain Belts

We consider a lithospheric column that initially consists of crust, thickness S, density ρ_c, and a mantle part, thickness L. If the thickness of the mantle portion of the lithosphere is reduced rapidly to $(1-\gamma)L$, the remainder of the mantle portion of the new column consists of asthenosphere of thickness $\gamma L + \Delta h$, density ρ_a (Figure B1). The

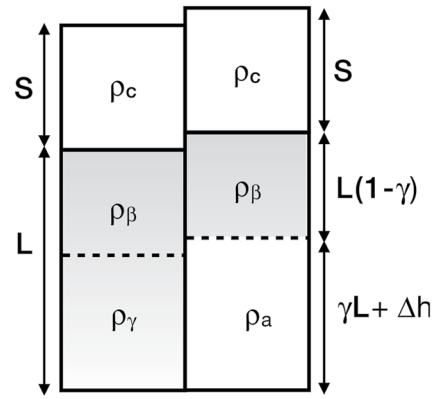

Figure B1. Definition sketch of change in density and potential energy associated with loss of lower lithosphere.

average density of the lithosphere that was removed is ρ_γ. We assume a constant density for the crust, and constant composition and temperature gradient throughout the lithospheric mantle, so the average densities of the different portions of the mantle depend upon γ and upon the temperature at the Moho, T_m, and of the asthenosphere, T_a.

$$\rho_a = \rho_m (1 - \alpha T_a), \tag{B1}$$

$$\rho_\beta = \rho_m \left(1 - \alpha \left(T_m + (1-\gamma)\frac{T_a - T_m}{2}\right)\right), \tag{B2}$$

$$\rho_\gamma = \rho_m \left(1 - \alpha \left(T_a - \gamma \frac{T_a - T_m)}{2}\right)\right), \tag{B3}$$

where α is the coefficient of thermal expansion.

The change in surface height assuming local isostasy is given by

$$\rho_\gamma \gamma L = \rho_a (\gamma L + \Delta h) \tag{B4}$$

$$\Delta h = \gamma L \left(\frac{\rho_\gamma}{\rho_a} - 1\right) \tag{B5}$$

$$\Delta h \approx \alpha \gamma^2 L \frac{\rho_m}{\rho_a} \left(\frac{T_a - T_m}{2}\right). \tag{B6}$$

Equation B6 reduces to Equation 2 of Molnar and Stock (2009) in their limit of $\gamma \to 1$. Note that surface height increases due to this mechanism are generally less than 1.5 km (Figure B2a).

From the sketch, the change in GPE is seen to consist of two parts: (a) an increase resulting from the uplift of the un-thinned lithosphere by Δh and (b) the difference in GPE between the denser lower lithosphere and the asthenosphere

$$\Delta\Gamma = g\Delta h (S\rho_c + L(1-\gamma)\rho_\beta) + g\rho_a \frac{(\gamma L + \Delta h)^2}{2} - g\rho_\gamma \frac{\gamma^2 L^2}{2} \tag{B7}$$

$$= g\Delta h (S\rho_c + L(1-\gamma)\rho_\beta) + \frac{g\rho_m\rho_\gamma}{\rho_a} \frac{\gamma^3 L^2 \alpha (T_a - T_m)}{4} \tag{B8}$$

where we have substituted for Δh in the second term using Equation B6, and the approximation consists of neglecting terms in Δh^2. These, and other small terms that would enter if we were to take full account of the variation of density with temperature in the mantle portion of the lithosphere, are negligible in comparison with the leading terms (Equation B8), and with uncertainties in the parameters. Comparison of contours of elevation change with contours of change in GPE in Figure B2a confirm that the relation proposed by Molnar and Stock (2009) ($\Delta\Gamma \sim 4\Delta h$ TN m^{-1}/km) remains appropriate.

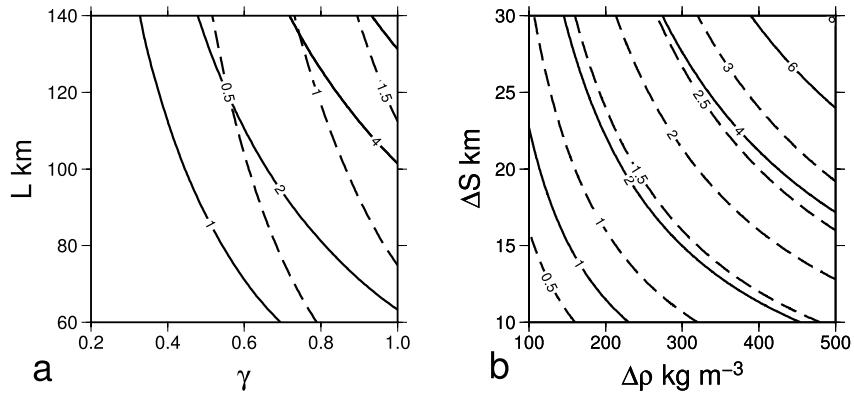

Figure B2. Variations in gravitational potential energy (GPE) due to loss of lower lithosphere or eclogitic lower crust. (a) Dependence of $\Delta\Gamma$ on fraction, γ, of mantle lithosphere lost and initial thickness, L, of mantle portion of lithosphere. Solid lines, annotated in TN m^{-1}, are contours of $\Delta\Gamma$ (Equation B8). Dashed lines, annotated in kilometers, are contours of Δh (Equation B6). (b) Dependence of $\Delta\Gamma$ (Equation B10) on density difference, $\Delta\rho$, between eclogitic lower crust and asthenosphere and thickness, ΔS, of crust removed. Annotations of contours as in (a). In each panel, the thickness of the crust after the change in density structure is 50 km.

The other potential cause of rise in surface height and GPE that we consider is convective instability of eclogitic lower crust (e.g., Jull & Kelemen, 2001). Suppose that thickness ΔS of eclogitic crust, having density contrast $\Delta\rho$ with the asthenosphere, were to be removed leaving crust of thickness S and density ρ_c.

$$\Delta h = \frac{\Delta\rho}{\rho_a}\Delta S, \tag{B9}$$

$$\Delta\Gamma = g\rho_c\Delta h S + \Delta\rho\left(1 + \frac{\Delta\rho}{\rho_a}\right)\frac{\Delta S^2}{2}, \tag{B10}$$

where we have assumed that no mantle lithosphere is present. Figure B2b shows that, whereas this mechanism is capable of causing surface height increase in excess of 2 km, the attendant increases in GPE are only about $\Delta\Gamma \sim 1.3\Delta h$ TN m^{-1}/km.

Data Availability Statement

All data used in this paper are from the published sources cited, apart from the Nazca-South America reconstructions of Garzione et al. (2006), which are given in Table A1. Data shown in Figure 1 come from (Garzione et al., 2006, given in Appendix A1) and DeMets and Merkouriev (2019). Data shown in Figure 4 come from DeMets and Merkouriev (2021). Table 1 is derived from (Garzione et al., 2006, given in Appendix A1), DeMets and Merkouriev (2019, 2021).

Acknowledgments
Most of the figures were prepared using the GMT package (Wessel and Smith, 2013). We are grateful to Laurent Husson and Bernhard Steinberger for thorough and helpful reviews, and to an Associate Editor for their comments. This study benefitted from discussions between Molnar and Chuck DeMets.

References

Argus, D. F., Gordon, R. G., & DeMets, C. (2011). Geologically current motion of 56 plates relative to the no-net-rotation reference frame. *Geochemistry, Geophysics, Geosystems*, *12*(11), Q11. https://doi.org/10.1029/2011gc003751

Austermann, J., Ben-Avraham, Z., Bird, P., Heidbach, O., Schubert, G., & Stock, J. M. (2011). Quantifying the forces needed for the rapid change of Pacific plate motion at 6 Ma. *Earth and Planetary Science Letters*, *307*(3–4), 289–297. https://doi.org/10.1016/j.epsl.2011.04.043

Backus, G., Park, J., & Garbasz, D. (1981). On the relative importance of the driving forces of plate motion. *Geophysical Journal International*, *67*(2), 415–435. https://doi.org/10.1111/j.1365-246x.1981.tb02758.x

Barke, R., & Lamb, S. (2006). Late Cenozoic uplift of the eastern Cordillera, Bolivian Andes. *Earth and Planetary Science Letters*, *249*(3–4), 350–367. https://doi.org/10.1016/j.epsl.2006.07.012

Bershaw, J., Garzione, C. N., Higgins, P., MacFadden, B. J., Anaya, F., & Alvarenga, H. (2010). Spatial–temporal changes in Andean Plateau climate and elevation from stable isotopes of mammal teeth. *Earth and Planetary Science Letters*, *289*(3–4), 530–538. https://doi.org/10.1016/j.epsl.2009.11.047

Bird, P. (1979). Continental delamination and the Colorado Plateau. *Journal of Geophysical Research*, *84*(B13), 7561–7571. https://doi.org/10.1029/jb084ib13p07561

Blisniuk, P. M., Hacker, B. R., Glodny, J., Ratschbacher, L., Bi, S., Wu, Z., et al. (2001). Normal faulting in central Tibet since at least 13.5 Myr ago. *Nature (London)*, *412*(6847), 628–632. https://doi.org/10.1038/35088045
Cande, S. C., & Stegman, D. R. (2011). Indian and African plate motions driven by the push force of the Réunion plume head. *Nature*, *475*(7354), 47–52. https://doi.org/10.1038/nature10174
Chang, T. (1986). Spherical regression. *Annals of Statistics*, *14*(3), 907–924. https://doi.org/10.1214/aos/1176350041
Chapple, W. M., & Tullis, T. E. (1977). Evaluation of the forces that drive the plates. *Journal of Geophysical Research*, *82*(14), 1967–1984. https://doi.org/10.1029/jb082i014p01967
Clark, M. K. (2012). Continental collision slowing due to viscous mantle lithosphere rather than topography. *Nature*, *483*(7387), 74–77. https://doi.org/10.1038/nature10848
Conrad, C. P., & Lithgow-Bertelloni, C. (2006). Influence of continental roots and asthenosphere on plate-mantle coupling. *Geophysical Research Letters*, *33*(5), L05312. https://doi.org/10.1029/2005GL025621
Conrad, C. P., & Molnar, P. (1997). The growth of Rayleigh-Taylor-type instabilities in the lithosphere for various rheological and density structures. *Geophysical Journal International*, *129*(1), 95–112. https://doi.org/10.1111/j.1365-246x.1997.tb00939.x
Conrad, C. P., & Molnar, P. (1999). Convective instability of a boundary layer with temperature-and strain-rate-dependent viscosity in terms of available buoyancy. *Geophysical Journal International*, *139*(1), 51–68. https://doi.org/10.1046/j.1365-246X.1999.00896.x
Copley, A., Avouac, J.-P., & Royer, J.-Y. (2010). India-Asia collision and the Cenozoic slowdown of the Indian plate: Implications for the forces driving plate motions. *Journal of Geophysical Research*, *115*(B03), 410. https://doi.org/10.1029/2009jb006634
DeMets, C., Gordon, R. G., & Royer, J.-Y. (2005). Motion between the Indian, Capricorn and Somalian plates since 20 Ma: Implications for the timing and magnitude of distributed lithospheric deformation in the equatorial Indian Ocean. *Geophysical Journal International*, *161*(2), 445–468. https://doi.org/10.1111/j.1365-246X.2005.02598.x
DeMets, C., & Merkouriev, S. (2019). High-resolution reconstructions of South America Plate Motion relative to Africa, Antarctica and North America: 34 Ma to present. *Geophysical Journal International*, *217*(3), 1821–1853. https://doi.org/10.1093/gji/ggz087
DeMets, C., & Merkouriev, S. (2021). Detailed reconstructions of India-Somalia plate motion, 60 Ma to present: Implications for Somalia plate absolute motion and India-Eurasia plate motion. *Geophysical Journal International*, ggab295. https://doi.org/10.1093/gji/ggab295
DeMets, C., Merkouriev, S., & Jade, S. (2020). High-resolution reconstructions and GPS estimates of India-Eurasia and India-Somalia Plate Motions: 20 Ma to the present. *Geophysical Journal International*, *220*(2), 1149–1171. https://doi.org/10.1093/gji/ggz508
DeMets, C., Merkouriev, S., & Sauter, D. (2021). High resolution reconstructions of the Southwest Indian Ridge, 52 Ma to present: Implications for the breakup and absolute motion of the Africa plate. *Geophysical Journal International*, *226*(3), 1461–1497. https://doi.org/10.1093/gji/ggab107
Dewey, J. F., Cande, S., & Pitman, W. C. (1989). Tectonic evolution of the India/Eurasia collision zone. *Eclogae Geologicae Helvetiae*, *82*, 717–734.
Dixon, N. A., & Durham, W. B. (2018). Measurement of activation volume for creep of dry olivine at upper-mantle conditions. *Journal of Geophysical Research: Solid Earth*, *123*(10), 8459–8473. https://doi.org/10.1029/2018JB015853
Echavarria, L., Hernández, R., Allmendinger, R., & Reynolds, J. (2003). Subandean thrust and fold belt of northwestern Argentina: Geometry and timing of the Andean evolution. *AAPG Bulletin*, *87*(6), 965–985. https://doi.org/10.1306/01200300196
Eiler, J. M. (2007). Clumped-isotope geochemistry—The study of naturally-occurring, multiply-substituted isotopologues. *Earth and Planetary Science Letters*, *262*(3–4), 309–327. https://doi.org/10.1016/j.epsl.2007.08.020
Elger, K., Oncken, O., & Glodny, J. (2005). Plateau-style accumulation of deformation: Southern Altiplano. *Tectonics*, 24. https://doi.org/10.1029/2004TC001675
Elliott, J. R., Walters, R. J., England, P. C., Jackson, J. A., Li, Z., & Parsons, B. (2010). Extension on the Tibetan Plateau: Recent normal faulting measured by InSAR and body wave seismology. *Geophysical Journal International*, *183*(2), 505–535. https://doi.org/10.1111/j.1365-246x.2010.04754.x
England, P., & Houseman, G. (1988). The mechanics of the Tibetan Plateau. *Philosophical Transactions of the Royal Society of London*, *326*, 301–320.
England, P., & Houseman, G. (1989). Extension during continental convergence, with application to the Tibetan Plateau. *Journal of Geophysical Research*, *94*, 17561–17579. https://doi.org/10.1029/jb094ib12p17561
England, P., & Searle, M. (1986). The Cretaceous–Tertiary deformation of the Lhasa block and its implications for crustal thickening in Tibet. *Tectonics*, *5*, 1–14. https://doi.org/10.1029/tc005i001p00001
Espurt, N., Barbarand, J., Roddaz, M., Brusset, S., Baby, P., Saillard, M., & Hermoza, W. (2011). A scenario for late Neogene Andean shortening transfer in the Camisea Subandean zone (Peru, 12 S): Implications for growth of the northern Andean Plateau. *The Geological Society of America Bulletin*, *123*(9–10), 2050–2068. https://doi.org/10.1130/B30165.1
Eude, A., Roddaz, M., Brichau, S., Brusset, S., Calderon, Y., Baby, P., & Soula, J.-C. (2015). Controls on timing of exhumation and deformation in the northern Peruvian eastern Andean wedge as inferred from low-temperature thermochronology and balanced cross section. *Tectonics*, *34*(4), 715–730. https://doi.org/10.1002/2014TC003641
Farías, M., Charrier, R., Carretier, S., Martinod, J., Fock, A., Campbell, D., et al. (2008). Late Miocene high and rapid surface uplift and its erosional response in the Andes of central Chile (33°–35°s). *Tectonics*, *27*(1), 22. https://doi.org/10.1029/2006tc002046
Farías, M., Charrier, R., Comte, D., Martinod, J., & Hérail, G. (2005). Late Cenozoic deformation and uplift of the western flank of the Altiplano: Evidence from the depositional, tectonic, and geomorphologic evolution and shallow seismic activity (northern Chile at 19°30'S). *Tectonics*, *24*(4). https://doi.org/10.1029/2004TC001667
Flesch, L., Haines, A., & Holt, W. (2001). Dynamics of the India-Eurasia collision zone. *Journal of Geophysical Research*, *106*, 16460. https://doi.org/10.1029/2001jb000208
Forsyth, D., & Uyeda, S. (1975). On the relative importance of the driving forces of plate motion. *Geophysical Journal International*, *43*(1), 163–200. https://doi.org/10.1111/j.1365-246x.1975.tb00631.x
Forte, A. M., Moucha, R., Rowley, D. B., Quéré, S., Mitrovica, J. X., Simmons, N. A., & Grand, S. P. (2009). Recent tectonic plate decelerations driven by mantle convection. *Geophysical Research Letters*, *36*(23), L23301. https://doi.org/10.1029/2009GL040224
Gaina, C., Roest, W., & Müller, R. (2002). Late Cretaceous–Cenozoic deformation of northeast Asia. *Earth and Planetary Science Letters*, *197*(3–4), 273–286. https://doi.org/10.1016/S0012-821X(02)00499-5
Gansser, A. (1980). The significance of the Himalayan suture zone. *Tectonophysics*, *62*(1–2), 37–52. https://doi.org/10.1016/0040-1951(80)90134-1
Garcia, M., & Hérail, G. (2005). Fault-related folding, drainage network evolution and valley incision during the Neogene in the Andean Precordillera of Northern Chile. *Geomorphology*, *65*(3–4), 279–300. https://doi.org/10.1016/j.geomorph.2004.09.007

Garver, J. I., Reiners, P. W., Walker, L. J., Ramage, J. M., & Perry, S. E. (2005). Implications for timing of Andean uplift from thermal resetting of radiation-damaged zircon in the Cordillera Huayhuash, Northern Peru. *The Journal of Geology*, *113*(2), 117–138. https://doi.org/10.1086/427664

Garzanti, E., Radeff, G., & Malusà, M. G. (2018). Slab breakoff: A critical appraisal of a geological theory as applied in space and time. *Earth-Science Reviews*, *177*, 303–319. https://doi.org/10.1016/j.earscirev.2017.11.012

Garzione, C. N., Auerbach, D. J., Smith, J. J.-S., Rosario, J. J., Passey, B. H., Jordan, T. E., & Eiler, J. M. (2014). Clumped isotope evidence for diachronous surface cooling of the Altiplano and pulsed surface uplift of the Central Andes. *Earth and Planetary Science Letters*, *393*, 173–181. https://doi.org/10.1016/j.epsl.2014.02.029

Garzione, C. N., Hoke, G. D., Libarkin, J. C., Withers, S., MacFadden, B., Eiler, J., et al. (2008). Rise of the Andes. *Science*, *320*(5881), 1304–1308. https://doi.org/10.1126/science.1148615

Garzione, C. N., Molnar, P., Libarkin, J. C., & MacFadden, B. J. (2006). Rapid late Miocene rise of the Bolivian Altiplano: Evidence for removal of mantle lithosphere. *Earth and Planetary Science Letters*, *241*(3–4), 543–556. https://doi.org/10.1016/j.epsl.2005.11.026

Gautheron, C., Espurt, N., Barbarand, J., Roddaz, M., Baby, P., Brusset, S., et al. (2013). Direct dating of thick- and thin-skin thrusts in the Peruvian Subandean zone through apatite (U-Th)/He and fission track thermochronometry. *Basin Research*, *25*(4), 419–435. https://doi.org/10.1111/bre.12012

Ge, W.-P., Molnar, P., Shen, Z.-K., & Li, Q. (2015). Present-day crustal thinning in the southern and northern Tibetan Plateau revealed by GPS measurements. *Geophysical Research Letters*, *42*(13), 5227–5235. https://doi.org/10.1002/2015gl064347

Ghosh, P., Garzione, C. N., & Eiler, J. M. (2006). Rapid uplift of the Altiplano Revealed through ^{13}C–^{18}O bonds in paleosol carbonates. *Science*, *311*(5760), 511–515. https://doi.org/10.1126/science.1119365

Gillis, R. J., Horton, B. K., & Grove, M. (2006). Thermochronology, geochronology, and upper crustal structure of the Cordillera Real: Implications for Cenozoic exhumation of the central Andean Plateau. *Tectonics*, *25*(6). https://doi.org/10.1029/2005TC001887

Giovanni, M., Horton, B., Garzione, C., McNulty, B., & Grove, M. (2010). Extensional basin evolution in the Cordillera Blanca, Peru: Stratigraphic and isotopic records of detachment faulting and orogenic collapse in the Andean hinterland. *Tectonics*, *29*(6). https://doi.org/10.1029/2010tc002666

Gregory-Wodzicki, K. M. (2002). A late Miocene subtropical-dry flora from the northern Altiplano, Bolivia. *Palaeogeography, Palaeoclimatology, Palaeoecology*, *180*(4), 331–348. https://doi.org/10.1016/s0031-0182(01)00434-5

Gregory-Wodzicki, K. M., Mcintosh, W. C., & Velasquez, K. (1998). Climatic and tectonic implications of the late Miocene Jakokkota flora, Bolivian Altiplano. *J. South Amer. Earth Sci.*, *11*, 533–560.

Gubbels, T. L., Isacks, B. L., & Farrar, E. (1993). High-level surfaces, plateau uplift, and foreland development, Bolivian central Andes. *Geology*, *21*(8), 695–698. https://doi.org/10.1130/0091-7613(1993)021<0695:hlspua>2.3.co;2

Hager, B. H., & O'Connell, R. J. (1981). A simple global model of plate dynamics and mantle convection. *Journal of Geophysical Research*, *86*(B6), 4843–4867. https://doi.org/10.1029/JB086iB06p04843

Harrison, T. M., Copeland, P., Kidd, W. S. F., & Lovera, O. M. (1995). Activation of the Nyainqentanghla Shear zone: Implications for uplift of the southern Tibetan Plateau. *Tectonics*, *14*(3), 658–676. https://doi.org/10.1029/95TC00608

Haschke, M., Günther, A., Melnick, D., Echtler, H., Reutter, K.-J., Scheuber, E., & Oncken, O. (2006). Central and southern Andean tectonic evolution inferred from arc magmatism, in the Andes. In O. Oncken, G. Chong, G. Franz, P. Giese, H.-J. Götze, V. A. Ramos, et al. (Eds.), *Frontiers in Earth sciences* (pp. 337–353). Springer Berlin Heidelberg. https://doi.org/10.1007/978-3-540-48684-8-16

Heidbach, O., Iaffaldano, G., & Bunge, H.-P. (2008). Topography growth drives stress rotations in the central Andes: Observations and models. *Geophysical Research Letters*, *35*(8), 905–906. https://doi.org/10.1029/2007gl032782

Hérail, G., Oller, J., Baby, P., Bonhomme, M., & Soler, P. (1996). Strike-slip faulting, thrusting and related basins in the Cenozoic evolution of the southern branch of the Bolivian Orocline. *Tectonophysics*, *259*(1–3), 201–212. https://doi.org/10.1016/0040-1951(95)00108-5

Hirth, G., & Kohlstedt, D. (2003). Rheology of the upper mantle and the mantle wedge: A view from the experimentalists. In J. Eiler & G. M. Ser (Eds.), *Inside the subduction factory* (Vol. 138, pp. 83–105). American Geophysical Union. https://doi.org/10.1029/138GM06

Hoke, G. D., & Garzione, C. N. (2008). Paleosurfaces, paleoelevations, and the mechanisms for the late Miocene topographic development of the Altiplano Plateau. *Earth and Planetary Science Letters*, *271*(1–4), 192–201. https://doi.org/10.1016/j.epsl.2008.04.008

Hoke, G. D., Isacks, B. L., Jordan, T. E., Blanco, N., Tomlinson, A. J., & Ramezani, J. (2007). Geomorphic evidence for post-10 Ma uplift of the western flank of the central Andes 18°30'–22°S. *Tectonics*, *26*(5), 17. https://doi.org/10.1029/2006tc002082

Houseman, G., McKenzie, D., & Molnar, P. (1981). Convective instability of a thickened boundary layer and its relevance for the thermal evolution of continental convergent belts. *Journal of Geophysical Research*, *86*(B7), 6115–6132. https://doi.org/10.1029/jb086ib07p06115

Houseman, G., & Molnar, P. (1997). Gravitational (Rayleigh–Taylor) instability of a layer with non-linear viscosity and convective thinning of continental lithosphere. *Geophysical Journal International*, *128*(1), 125–150. https://doi.org/10.1111/j.1365-246x.1997.tb04075.x

Hungerbühler, D., Steinmann, M., Winkler, W., Seward, D., Egüez, A., Peterson, D. E., et al. (2002). Neogene stratigraphy and Andean geodynamics of southern Ecuador. *Earth-Science Reviews*, *57*(1–2), 75–124. https://doi.org/10.1016/S0012-8252(01)00071-X

Iaffaldano, G., & Bunge, H.-P. (2009). Relating rapid plate-motion variations to plate-boundary forces in global coupled models of the mantle/lithosphere system: Effects of topography and friction. *Tectonophysics*, *474*(1–2), 393–404. https://doi.org/10.1016/j.tecto.2008.10.035

Iaffaldano, G., Bunge, H.-P., & Dixon, T. H. (2006). Feedback between mountain belt growth and plate convergence. *Geology*, *34*(10), 893–894. https://doi.org/10.1130/g22661.1

Isacks, B., Oliver, J., & Sykes, L. (1968). Seismology and the new global tectonics. *Journal of Geophysical Research*, *73*(5–6), 5855–5899. https://doi.org/10.1016/0040-1951(69)90024-9

Jordan, T. E., Allmendinger, R. W., Damanti, J. F., & Drake, R. E. (1993). Chronology of motion in a complete thrust belt: The Precordillera, 30–31°S, Andes Mountains thrust belt. *The Journal of Geology*, *101*(2), 135–156. https://doi.org/10.1086/648213

Jordan, T. E., Nester, P. L., Blanco, N., Hoke, G. D., Dávila, F., & Tomlinson, A. J. (2010). Uplift of the Altiplano-Puna Plateau: A view from the west. *Tectonics*, *29*(5). https://doi.org/10.1029/2010TC002661

Jull, M., & Kelemen, P. B. (2001). On the conditions for lower crustal convective instability. *Journal of Geophysical Research*, *106*(B4), 6423–6446. https://doi.org/10.1029/2000JB900357

Kapp, P., DeCelles, P., Leier, A., Fabijanic, J., He, S., Pullen, A., et al. (2007). The Gangdese retroarc thrust belt revealed. *Geological Society of America Today*, *17*(7), 4. https://doi.org/10.1130/GSAT01707A.1

Kapp, P., DeCelles, P. G., Gehrels, G. E., Heizler, M., & Ding, L. (2007b). Geological records of the Lhasa-Qiangtang and Indo-Asian collisions in the Nima area of central Tibet. *The Geological Society of America Bulletin*, *119*(7–8), 917–933. https://doi.org/10.1130/B26033.1

Kapp, P., Murphy, M. A., Yin, A., Harrison, T. M., Ding, L., & Guo, J. (2003). Mesozoic and Cenozoic tectonic evolution of the Shiquanhe area of western Tibet. *Tectonics*, *22*(4). https://doi.org/10.1029/2001TC001332

Kapp, P., Yin, A., Harrison, T. M., & Ding, L. (2005). Cretaceous-Tertiary shortening, basin development, and volcanism in central Tibet. *The Geological Society of America Bulletin*, *117*(7), 865. https://doi.org/10.1130/b25595.1

Kar, N., Garzione, C. N., Jaramillo, C., Shanahan, T., Carlotto, V., Pullen, A., et al. (2016). Rapid regional surface uplift of the northern Altiplano Plateau revealed by multiproxy paleoclimate reconstruction. *Earth and Planetary Science Letters*, *447*, 33–47. https://doi.org/10.1016/j.epsl.2016.04.025

Kay, R. W., & Mahlburg Kay, S. (1991). Creation and destruction of lower continental crust. *Geologische Rundschau*, *80*(2), 259–278. https://doi.org/10.1007/BF01829365

Kennan, L., Lamb, S., & Hoke, L. (1997). High-altitude palaeosurface in the Bolivian Andes: Evidence for late Cenozoic surface uplift. In M. Widdowson (Ed.), *Palaeosurfaces: Recognition, reconstruction and palaeoenvironmental interpretation* (Vol. 120, pp. 307–323). Geological Society London.

Kley, J. (1996). Transition from basement-involved to thin-skinned thrusting in the Cordillera Oriental of southern Bolivia. *Tectonics*, *15*(4), 763–775. https://doi.org/10.1029/95TC03868

Kley, J., Müller, J., Tawackoli, S., Jacobshagen, V., & Manutsoglu, E. (1997). Pre-Andean and Andean-age deformation in the eastern Cordillera of southern Bolivia. *Journal of South American Earth Sciences*, *10*, 1–19. https://doi.org/10.1016/S0895-9811(97)00001-1

Lease, R. O., Ehlers, T. A., & Enkelmann, E. (2016). Large along-strike variations in the onset of Subandean exhumation: Implications for Central Andean orogenic growth. *Earth and Planetary Science Letters*, *451*, 62–76. https://doi.org/10.1016/j.epsl.2016.07.004

Leeder, M., Smith, A., & Yin, J. (1988). Sedimentology, palaeoecology and palaeoenvironmental evolution of the 1985 Lhasa to Golmud Geotraverse. In *Series A, mathematical and physical sciences* (Vol. 327, pp. 107–143). Philosophical Transactions of the Royal Society of London. https://doi.org/10.1098/rsta.1988.0123

Levina, M., Horton, B. K., Fuentes, F., & Stockli, D. F. (2014). Cenozoic sedimentation and exhumation of the foreland basin system preserved in the Precordillera thrust belt (31–32°S), southern central Andes, Argentina: Precordillera thrust belt evolution. *Tectonics*, *33*(9), 1659–1680. https://doi.org/10.1002/2013TC003424

Li, L., Garzione, C. N., Pullen, A., Zhang, P., & Li, Y. (2018). Late Cretaceous–Cenozoic basin evolution and topographic growth of the Hoh Xil Basin, central Tibetan Plateau. *GSA Bulletin*, *130*(3–4), 499–521. https://doi.org/10.1130/B31769.1

Li, Y., Wang, C., Ma, C., Xu, G., & Zhao, X. (2011). Balanced cross-section and crustal shortening analysis in the Tanggula-Tuotuohe area, northern Tibet. *Journal of Earth Sciences*, *22*, 1–10. https://doi.org/10.1007/s12583-011-0152-2

Li, Y., Wang, C., Zhao, X., Yin, A., & Ma, C. (2012). Cenozoic thrust system, basin evolution, and uplift of the Tanggula Range in the Tuotuohe region, central Tibet. *Gondwana Research*, *22*(2), 482–492. https://doi.org/10.1016/j.gr.2011.11.017

Lister, C. (1975). Gravitational drive on oceanic plates caused by thermal contraction. *Nature*, *257*(5528), 663–665. https://doi.org/10.1038/257663a0

Lithgow-Bertelloni, C., & Richards, M. A. (1995). Cenozoic plate driving forces. *Geophysical Research Letters*, *22*(11), 1317–1320. https://doi.org/10.1029/95GL01325

Lithgow-Bertelloni, C., & Richards, M. A. (1998). The dynamics of Cenozoic and Mesozoic plate motions. *Reviews of Geophysics*, *36*(1), 27–78. https://doi.org/10.1029/97RG02282

Lithgow-Bertelloni, C., & Silver, P. (1998). Dynamic topography, plate driving forces and the African superswell. *Nature*, *395*(6699), 269–272. https://doi.org/10.1038/26212

Mackaman-Lofland, C., Horton, B. K., Fuentes, F., Constenius, K. N., Ketcham, R. A., Capaldi, T. N., et al. (2020). Andean mountain building and foreland basin evolution during thin- and thick-skinned Neogene deformation (32–33°S). *Tectonics*, 39. https://doi.org/10.1029/2019TC005838

Margirier, A., Audin, L., Robert, X., Herman, F., Ganne, J., & Schwartz, S. (2016). Time and mode of exhumation of the Cordillera Blanca Batholith (Peruvian Andes). *Journal of Geophysical Research: Solid Earth*, *121*(8), 6235–6249. https://doi.org/10.1002/2016JB013055

Martínez, C., Jaramillo, C., Correa-Metrío, A., Crepet, W., Moreno, J. E., Aliaga, A., et al. (2020). Neogene precipitation, vegetation, and elevation history of the Central Andean Plateau. *Science Advances*, *6*(35), eaaz4724. https://doi.org/10.1126/sciadv.aaz4724

Martinod, J., Gérault, M., Husson, L., & Regard, V. (2020). Widening of the Andes: An interplay between subduction dynamics and crustal wedge tectonics. *Earth-Science Reviews*, *204*, 103–170. https://doi.org/10.1016/j.earscirev.2020.103170

Martinod, J., Husson, L., Roperch, P., Guillaume, B., & Espurt, N. (2010). Horizontal subduction zones, convergence velocity and the building of the Andes. *Earth and Planetary Science Letters*, *299*(3–4), 299–309. https://doi.org/10.1016/j.epsl.2010.09.010

McCallister, A. T., Taylor, M. H., Murphy, M. A., Styron, R. H., & Stockli, D. F. (2014). Thermochronologic constraints on the late Cenozoic exhumation history of the Gurla Mandhata metamorphic core complex, southwestern Tibet. *Tectonics*, *33*(2), 27–52. https://doi.org/10.1002/2013tc003302

Molnar, P. (2022). The rise of the Tibetan Plateau and removal of some of its mantle lithosphere in light of recent observations. *Himalayan Geology*, *43*, 1123–1139.

Molnar, P., England, P., & Martinod, J. (1993). Mantle dynamics, uplift of the Tibetan Plateau, and the Indian monsoon. *Reviews of Geophysics*, *31*(4), 357–396. https://doi.org/10.1029/93rg02030

Molnar, P., & Gray, D. (1979). Subduction of continental lithosphere: Some constraints and uncertainties. *Geology*, *7*(1), 58–62. https://doi.org/10.1130/0091-7613(1979)7<58:soclsc>2.0.co;2

Molnar, P., Houseman, G., & Conrad, C. (1998). Rayleigh–Taylor instability and convective thinning of mechanically thickened lithosphere: Effects of non-linear viscosity decreasing exponentially with depth and of horizontal shortening of the layer. *Geophysical Journal International*, *133*(3), 568–584. https://doi.org/10.1046/j.1365-246x.1998.00510.x

Molnar, P., & Lyon-Caen, H. (1988). Some simple physical aspects of the support, structure, and evolution of mountain belts. In S. P. ClarkJr., B. C. Burchfiel, & J. Suppe (Eds.), *Processes in continental lithospheric deformation* (Vol. 218, pp. 179–207). The Geological Society of America.

Molnar, P., & Stock, J. M. (2009). Slowing of India's convergence with Eurasia since 20 Ma and its implications for Tibetan mantle dynamics. *Tectonics*, *28*(3). https://doi.org/10.1029/2008tc002271

Molnar, P., & Tapponnier, P. (1975). Cenozoic tectonics of Asia: Effects of a continental collision. *Science*, *189*(4201), 419–426. https://doi.org/10.1126/science.189.4201.419

Moreno, F., Garzione, C. N., George, S. W. M., Horton, B. K., Williams, L., Jackson, L. J., et al. (2020). Coupled Andean growth and foreland basin evolution, Campanian–Cenozoic Bagua basin, northern Peru. *Tectonics*, *39*(7). https://doi.org/10.1029/2019TC005967

Nelson, K. D. (1992). Are crustal thickness variations in old mountain belts like the Appalachians a consequence of lithospheric delamination? *Geology*, *20*(6), 498. https://doi.org/10.1130/0091-7613

Norabuena, E. O., Dixon, T., Stein, S., & Harrison, C. G. A. (1999). Decelerating Nazca-South America and Nazca-Pacific plate motions. *Geophysical Research Letters*, *26*(22), 3405–3408. https://doi.org/10.1029/1999gl005394

Pan, Y., & Kidd, W. (1992). Nyainqentanglha shear zone: A late Miocene extensional detachment in the southern Tibetan Plateau. *Geology*, *20*, 775. https://doi.org/10.1130/0091-7613

Patriat, P., & Achache, J. (1984). India–Eurasia collision chronology has implications for crustal shortening and driving mechanism of plates. *Nature*, *311*(5987), 615–621. https://doi.org/10.1038/311615a0

Platt, J. P., & England, P. C. (1994). Convective removal of lower lithosphere beneath mountain belts, thermal and mechanical consequences. *American Journal of Science*, *294*(3), 307–336. https://doi.org/10.2475/ajs.294.3.307

Quade, J., Dettinger, M., Carrapa, B., DeCelles, P., Murray, K., Huntington, K., et al. (2015). The growth of the central Andes, 22°S–26°S. In *Geodynamics of a cordilleran orogenic system: The central Andes of Argentina and northern Chile*. Geological Society of America. https://doi.org/10.1130/2015.1212(15

Quiero, F., Tassara, A., Iaffaldano, G., & Rabbia, O. (2022). Growth of Neogene Andes linked to changes in plate convergence using high-resolution kinematic models. *Nature Communications*, *13*(1), 1339. https://doi.org/10.1038/s41467-022-29055-4

Richards, M. A., & Lithgow-Bertelloni, C. (1996). Plate motion changes, the Hawaiian-Emperor bend, and the apparent success and failure of geodynamic models. *Earth and Planetary Science Letters*, *137*(1–4), 19–27. https://doi.org/10.1016/0012-821X(95)00209-U

Schettino, A., & Macchiavelli, C. (2016). Plate kinematics of the central Atlantic during the Oligocene and early Miocene. *Geophysical Journal International*, *205*(1), 408–426. https://doi.org/10.1093/gji/ggw022

Scheuber, E., Mertmann, D., Ege, H., Silva-González, P., Heubeck, C., Reutter, K.-J., & Jacobshagen, V. (2006). Exhumation and basin development related to formation of the central Andean Plateau, 21°S, in the Andes. In O. Oncken, G. Chong, G. Franz, P. Giese, H.-J. Götze, V. A. Ramos, et al. (Eds.), *Frontiers in Earth sciences* (pp. 285–301). Springer Berlin Heidelberg. https://doi.org/10.1007/978-3-540-48684-8-13

Schildgen, T. F., Ehlers, T. A., Whipp, D. M., Soest, M. C. V., Whipple, K. X., & Hodges, K. V. (2009). Quantifying canyon incision and Andean Plateau surface uplift, southwest Peru: A thermochronometer and numerical modeling approach. *Journal of Geophysical Research*, *114*(F4), 1–22. https://doi.org/10.1029/2009jf001305

Schildgen, T. F., Hodges, K. V., Whipple, K. X., Reiners, P. W., & Pringle, M. S. (2007). Uplift of the western margin of the Andean Plateau revealed from canyon incision history, southern Peru. *Geology*, *35*(6), 523. https://doi.org/10.1130/G23532A.1

Schoenbohm, L. M., & Carrapa, B. (2015). Miocene–Pliocene shortening, extension, and mafic magmatism support small-scale lithospheric foundering in the central Andes, NW Argentina. In *Geodynamics of a cordilleran orogenic system: The central Andes of Argentina and northern Chile*. Geological Society of America. https://doi.org/10.1130/2015.121209

Schoenbohm, L. M., & Strecker, M. R. (2009). Normal faulting along the southern margin of the Puna Plateau, northwest Argentina. *Tectonics*, *28*(5). https://doi.org/10.1029/2008TC002341

Spikings, R., Crowhurst, P., Winkler, W., & Villagomez, D. (2010). Syn- and post-accretionary cooling history of the Ecuadorian Andes constrained by their in-situ and detrital thermochronometric record. *Journal of South American Earth Sciences*, *30*(3–4), 121–133. https://doi.org/10.1016/j.jsames.2010.04.002

Staisch, L. M., Niemi, N. A., Clark, M. K., & Chang, H. (2016). Eocene to late Oligocene history of crustal shortening within the Hoh Xil Basin and implications for the uplift history of the northern Tibetan Plateau. *Tectonics*, *35*(4), 862–895. https://doi.org/10.1002/2015tc003972

Staisch, L. M., Niemi, N. A., Hong, C., Clark, M. K., Rowley, D. B., & Currie, B. (2014). A Cretaceous-Eocene depositional age for the Fenghuoshan Group, Hoh Xil Basin: Implications for the tectonic evolution of the northern Tibet Plateau. *Tectonics*, *33*(3), 281–301. https://doi.org/10.1002/2013TC003367

Steinberger, B. (2000). Plumes in a convecting mantle: Models and observations for individual hotspots. *Journal of Geophysical Research*, *105*(B5), 11127–11152. https://doi.org/10.1029/1999JB900398

Steinmann, M., Hungerbühler, D., Seward, D., & Winkler, W. (1999). Neogene tectonic evolution and exhumation of the southern Ecuadorian Andes: A combined stratigraphy and fission-track approach. *Tectonophysics*, *307*(3–4), 255–276. https://doi.org/10.1016/S0040-1951(99)00100-6

Stock, J., & Molnar, P. (1983). Some geometrical aspects of uncertainties in combined plate reconstructions. *Geology*, *11*(12), 697–701. https://doi.org/10.1130/0091-7613

Styron, R. H., Taylor, M. H., Sundell, K. E., Stockli, D. F., Oalmann, J. A. G., Möller, A., et al. (2013). Miocene initiation and acceleration of extension in the South Lunggar rift, western Tibet: Evolution of an active detachment system from structural mapping and (U-Th)/He thermochronology. *Tectonics*, *32*, 880–907. https://doi.org/10.1002/tect.20053

Tebbens, S. F., Cande, S. C., Kovacs, L., Parra, J. C., LaBrecque, J. L., & Vergara, H. (1997). The Chile ridge: A tectonic framework. *Journal of Geophysical Research*, *102*, 12035–12059. https://doi.org/10.1029/96JB02581

Thouret, J.-C., Wörner, G., Gunnell, Y., Singer, B., Zhang, X., & Souriot, T. (2007). Geochronologic and stratigraphic constraints on canyon incision and Miocene uplift of the Central Andes in Peru. *Earth and Planetary Science Letters*, *263*(3–4), 151–166. https://doi.org/10.1016/j.epsl.2007.07.023

Torsvik, T. H., Steinberger, B., Gurnis, M., & Gaina, C. (2010). Plate tectonics and net lithosphere rotation over the past 150 My. *Earth and Planetary Science Letters*, *291*(1–4), 106–112. https://doi.org/10.1016/j.epsl.2009.12.055

van Hinsbergen, D. J. J., Steinberger, B., Doubrovine, P. V., & Gassmöller, R. (2011). Acceleration and deceleration of India-Asia convergence since the Cretaceous: Roles of mantle plumes and continental collision. *Journal of Geophysical Research*, *116*(B6), B06101. https://doi.org/10.1029/2010JB008051

Vergnolle, M., Calais, E., & Dong, L. (2007). Dynamics of continental deformation in Asia. *Journal of Geophysical Research*, *112*(B11), 22. https://doi.org/10.1029/2006jb004807

Volkmer, J. E., Kapp, P., Guynn, J. H., & Lai, Q. (2007). Cretaceous-Tertiary structural evolution of the north central Lhasa terrane, Tibet. *Tectonics*, *26*(6), 18. https://doi.org/10.1029/2005tc001832

Volkmer, J. E., Kapp, P., Horton, B. K., Gehrels, G. E., Minervini, J. M., & Ding, L. (2014). Northern Lhasa thrust belt of central Tibet: Evidence of Cretaceous–early Cenozoic shortening within a passive roof thrust system? In *Toward an improved understanding of uplift mechanisms and the elevation history of the Tibetan Plateau*. Geological Society of America. https://doi.org/10.1130/2014.2507(03

Wang, C., Liu, Z., Yi, H., Liu, S., & Zhao, X. (2002). Tertiary crustal shortening and peneplanation in the Hoh Xil region: Implications for the tectonic history of the northern Tibetan Plateau. *Journal of Asian Earth Sciences*, *20*(3), 211–223. https://doi.org/10.1016/S1367-9120(01)00051-7

Wang, C., Zhao, X., Liu, Z., Lippert, P., Graham, S., Coe, R., et al. (2008). Constraints on the early uplift history of the Tibetan Plateau. *Proceedings of the National Academy of Sciences*, *105*(13), 4987–4992. https://doi.org/10.1073/pnas.0703595105

Wessel, P., Smith, W. H. F., Scharroo, R., Luis, J., & Wobbe, F. (2013). Generic mapping tools: Improved version released. *Eos, Transactions American Geophysical Union*, *94*(45), 409–410. https://doi.org/10.1002/2013eo450001

Wolff, R., Hetzel, R., Dunkl, I., Xu, Q., Bröcker, M., & Anczkiewicz, A. A. (2019). High-angle normal faulting at the Tangra Yumco Graben (Southern Tibet) since ~15 Ma. *The Journal of Geology*, *127*(1), 15–36. https://doi.org/10.1086/700406

Woodruff, W. H., Horton, B. K., Kapp, P., & Stockli, D. F. (2013). Late Cenozoic evolution of the Lunggar extensional basin, Tibet: Implications for basin growth and exhumation in hinterland Plateaus. *The Geological Society of America Bulletin*, *125*(3–4), 343–358. https://doi.org/10.1130/b30664.1

Wu, Z., Barosh, P. J., Wu, Z., Hu, D., Zhao, X., & Ye, P. (2008). Vast early Miocene lakes of the central Tibetan Plateau. *The Geological Society of America Bulletin*, *120*(9–10), 1326–1337. https://doi.org/10.1130/B26043.1

Wu, Z., Ye, P., Barosh, P. J., Hu, D., Lu, L., & Zhang, Y. (2012). Early Cenozoic mega thrusting in the Qiangtang block of the northern Tibetan Plateau. *Acta Geologica Sinica—English Edition*, *86*(4), 799–809. https://doi.org/10.1111/j.1755-6724.2012.00707.x

Yakovlev, P. V., & Clark, M. K. (2014). Conservation and redistribution of crust during the Indo-Asian collision. *Tectonics*, *33*(6), 1016–1027. https://doi.org/10.1002/2013tc003469